Effects of Biophysical and Physiologic Parameters on Brain Activation-Induced R_2^* and R_2 Changes: Simulations Using a Deterministic Diffusion Model

Peter A. Bandettini

MGH–NMR Center, Department of Radiology, Massachusetts General Hospital and Harvard Medical School, Charlestown, MA 02129

Eric C. Wong

Departments of Radiology and Psychiatry, University of California–San Diego, San Diego, CA 92103

ABSTRACT

A central issue in magnetic resonance imaging of human brain function using blood oxygenation level–dependent (BOLD) contrast is the accurate interpretation of the signal changes that are observed. Using a method that incorporates repeated phase rotation and convolution with a smoothing function to simulate spin diffusion in the presence of magnetic field perturbers, the dependencies of the absolute and relative changes in transverse relaxation rates (ΔR_2^* and ΔR_2) on biophysical and physiologic parameters were explored. First we introduce the modeling methodology. Then we simulate ΔR_2^* and ΔR_2 as physiologic and biophysical parameters are modulated within the ranges that they vary across subjects and voxels in the brain. The simulations demonstrate that the ΔR_2^* and ΔR_2 values that occur with activation-induced changes in blood oxygenation depend most strongly on the resting state blood volume and field strength. The $\Delta R_2^*/\Delta R_2$ ratios depend most strongly on the vessel radius and spin diffusion coefficient. © 1995 John Wiley & Sons, Inc.

I. INTRODUCTION

A goal in functional magnetic resonance imaging (FMRI) is the complete understanding of the relationship between brain activation and the observed MR signal changes. In pursuit of this goal, biophysical models that are based on the current understanding of cerebral hemodynamics, blood susceptibility, proton dynamics, and MR physics have been formulated. The model formulation and testing process can give insight into the factors that contribute to the observed activation-induced MR signal changes, and may eventually lead to a quantifiable correlation between the observed signal changes and the underlying neuronal processes.

Several models describing brain activation-induced blood oxygenation level–dependent (BOLD) MR signal changes have been published. The models of Ogawa et al. [1], Weisskoff et al. [2, 3], Kennan et al. [4], Yablonsky et al. [5], and Boxerman et al. [6–9] are particularly instructive in describing specific aspects of BOLD contrast. Most of the models consider two fundamental variables in the context of BOLD contrast: magnetic field perturbers and proton dynamics.

Red blood cells and blood vessels are considered here to be magnetic field perturbers. They have a magnetic susceptibility that is sensitive to the oxygen saturation of hemoglobin. During brain activation, the oxygen saturation of hemoglobin is thought to increase locally, causing the magnetic susceptibility of the perturbers to decrease.

The dynamics of protons in the vicinity of these perturbers affects the relative manner in which irreversible (T_2-related) and reversible (T_2^*-related) dephasing takes place. In the context of FMRI-related spin dephasing effects, proton diffusion has been considered to be the most relevant dynamic process. In the models mentioned above, these diffusion effects are simulated using random walk (Monte Carlo) methods. The positions of the individual spins are tracked over time and their phase histories are recorded.

In this study, diffusion was simulated by a deterministic technique first introduced by Wong et al. [10]. This technique uses the convolution of a spin density map with a smoothing function, and is deterministic in that no random variables are used.

In this article we describe a simple biophysical model which is based on first-order approximations of resting and active state cerebral hemodynamics, vessel architecture, blood oxygenation, and proton dynamics. The fundamental variables that are considered include: a) the susceptibility-induced frequency shift, which is modulated by blood oxygenation, magnetic field strength, and hematocrit; b) the vessel geometry, which includes vessel radii, vessel orientation, and blood volume; and c) the diffusion coefficient, which is considered here to be isotropic and unrestricted. The relative and absolute effects of varying these factors on ΔR_2 (spin-echo) and ΔR_2^* (gradient-echo) signal are compared with the experimental results reported in literature.

As a review, the rationale behind the choice of physiologic and biophysical variables in the modeling process is first discussed. Second, the relationships, as they have been

International Journal of Imaging Systems and Technology, Vol. 6, 133–152 (1995)
© 1995 John Wiley & Sons, Inc.
CCC 0899–9457/95/02/30133–20

presented in the literature, between blood oxygenation and spin precession frequency in the vicinity of the particular geometry chosen (infinite cylinder) are then described. Third, the details of formulation and implementation of the deterministic biophysical model are given. Fourth, an example is presented to illustrate the salient details of the model. Fifth, validation of the deterministic modeling method is carried out by comparison with results of Ogawa et al. [1] who used Monte Carlo methods to simulate spin diffusion. Lastly, several physiologic and biophysical parameters are modulated and the effects on the simulated R_2 and R_2^* are observed.

II. MODELING CONSIDERATIONS

When attempting to model a physical phenomena, it is ideal to have all of the model parameters accurately represented. Then, the relative significance of each parameter can be precisely determined by repeated simulations in which each parameter value is modulated, keeping all other parameters constant. However, in this particular modeling problem, almost all of the parameters (concerning cerebral hemodynamics, blood oxygenation, and proton dynamics) are imprecisely known, and the relative contribution of each parameter to the activation-induced MR signal changes is not clearly understood. These variables may also vary from voxel to voxel in space. Under these circumstances, the applicability of the model was evaluated by determining whether the simulated results agreed with absolute and relative activation-induced ΔR_2^* and ΔR_2 values described in the literature. The relative importance of the various parameters was evaluated by varying one parameter at a time, keeping all the other parameters constant.

A. Resting State Physiologic Considerations

1. Hemoglobin Saturation. The susceptibility of blood is linearly proportional to the fractional hemoglobin saturation, Y [11]. As blood passes through microvessels in the vicinity of metabolically active cerebral tissue, oxygen is delivered to the tissue, causing the partial pressure of oxygen in the blood (pO_2) to decrease from approximately 95 to 30 mm Hg [12]. The relationship between pO_2 and Y is approximately given by [13]:

$$Y/(1-Y) = (pO_2/P_{50})^{2.8} \tag{1}$$

where P_{50}, the pO_2 at which $Y = 0.5$, equals 26 mm Hg [14]. The fractional saturation of hemoglobin is therefore reduced from 0.97 (arterial side) to 0.59 (venous side) as blood passes through the capillary bed. In the simulations we assume that the MR signal is primarily affected by blood oxygenation changes in the venous end of the capillaries, venuoles, collecting veins, and pial veins. We therefore use a resting Y value of 0.6.

2. Vessel Radius. As described in a study by Duvernoy et al. [15] of the anatomic structure of the human cerebral vasculature, vessel radii vary considerably: central pial arteries, 130–140 μm; peripheral pial arteries, 75–90 μm; arterioles at the cortex surface, $\leq$25 μm; arteriol anastomoses (connecting arterioles), 12–45 μm. Arteries that penetrate the cortical surface have diameters generally dependent on the depth of penetration. Their diameters at the base range from 120 μm (deepest arterioles) to 5 μm (most shallow arterioles).

Other vessel radii also vary: central pial veins, 140–190 μm, peripheral pial veins, 60 μm; the largest principle veins (largest intracortical vein), 40–62 μm. As a side note, principle veins generally penetrate the cortex in a perpendicular manner and drain surrounding cortical areas within a radius of 0.5–2 mm. Considering a cortical thickness of 3 mm, the draining volume would be 0.75–12 mm^3. Other draining veins have radii which depend on their depth of penetration and cortical drainage area. In the largest of these, the radii are 32 μm. In the smallest, the radii are 10 μm. Other cortical veins branch out tangentially and have radii similar to those of draining veins.

Capillaries have radii ranging from 2.5–4 μm. Capillary orientation is generally random, but shows some orientation preference in several cortical layers (I, tangental to cortex surface; II, palisading, IV, tangential).

In the simulations presented subsequently, the vessel radius is varied from 2.5–20 μm. Above 20 μm, as will be discussed, the diffusion effects are minimal and $\Delta R_2^*/\Delta R_2$ approaches infinity, therefore obviating the need to increase simulated radii further. When keeping the radius constant and varying other parameters, we chose a radius of 10 μm for the simulations. The motivation for this choice is related to the fact that when simulation results of Ogawa et al. [Figure 6 of (1)] are compared with data presented in the literature [16–22], which generally give an $\Delta R_2^*/\Delta R_2$ ratio between 3/1 and 4/1, the "average" vessel size comes out to be about 10 μm. The simulations presented here also show general agreement with this result. In these preliminary simulations an "average" compartment size (or vessel radius) was chosen with the understanding that it represented a weighted combination of radii ranging from 2.5 μm (capillaries and red blood cells within larger vessels) to 190 μ (central pial veins).

3. Vessel Orientation. As mentioned earlier, the cerebral vasculature has some structure and orientation relative to the cortical surface. The larger the vessel, the more likely that it will display a single orientation in a voxel. The relative effects on relaxation rate changes by variation of vessel angle were observed in one simulation. In all other simulations, a random vessel orientation distribution, ranging from 0 to $\pi/2$, was used.

4. Blood Volume. The cerebral blood volumes that are used in many simulations are in the range of 2–5%. One caveat to this assumption is that if the brain is divided into voxels, as for an imaging experiment, the fraction of the voxel that is blood may vary widely. It is likely that the heterogeneity in the distribution of blood volume in each voxel is smallest for the smallest vessels and largest for larger vessels. It can be assumed that capillary blood volume, about half of the total cerebral blood volume, is homogeneously distributed across voxels. In larger vessels, it is very likely that a single vessel may completely fill several voxels, giving a 100% blood volume. In general, larger vessels that change in oxygenation may give a very large signal change simply because of the large blood volume in those particular voxels.

Simulations of the relative effects on activation-induced signal changes by variations in resting state blood volume were carried out. When other parameters were varied, we used a fractional blood volume value of 4%. It was under-

stood that 80% of the total cerebral blood volume is contained in veins and capillaries [23]. As will be discussed later, activation-induced changes in oxygenation occur primarily in veins and capillaries. Assuming a total (arteries, capillaries, and veins) fractional blood volume of 5%, it is therefore reasonable to use the value of 4% to account for the capillary and venous blood being considered.

5. Hematocrit. The average hematocrit in healthy humans falls in the range of 30–50 (i.e., 30%–50% of blood volume consists of red blood cells), but varies considerably in vivo with vessel diameter [23]. It may vary from 50 in the largest vessels to as low as 30 in capillaries. In these simulations, a hematocrit of 42 was used.

6. Proton Dynamics. The final model consideration is that of proton dynamics in the presence of magnetic field perturbers. Proton dynamics include diffusion, exchange across red blood cell membranes, and exchange across capillary walls. Also, movement of red blood cells relative to protons may be considered to be proton dynamics, because the extent of dephasing depends on relative and not absolute dynamics. The diffusion coefficient of free water has been measured to be about 2.5 $\mu m^2/ms$ [24, 25]. In contrast, the diffusion coefficient of protons in the brain was measured to be 1 $\mu m^2/ms$ [26]. Diffusion in gray matter may also be restricted and anisotropic. The average velocity of red blood cells is about 0.3 mm/s in the capillaries [15, 23].

In the simulations performed, the relative relaxation rate changes are observed as the diffusion coefficient is varied. When other parameters are varied, the diffusion coefficient was set equal to 1 $\mu m^2/ms$. Diffusion was also considered to be unrestricted and isotropic.

B. Activation-Related Physiologic Considerations. During cerebral activation, neuronal and subsequent hemodynamic events take place. Through incompletely understood mechanisms [23, 27–51], arteriolar sphincters open, causing an increase in blood flow. This increase in blood flow is generally accompanied by capillary recruitment, venous vessel distention, and an increase in flow velocity where vessels neither distend nor are recruited. Despite these marked flow changes, it has been demonstrated that the oxidative metabolic rate does not increase proportionally [48] during brain activation.

As discussed by Weisskoff et al. [3], the relationship between resting and activated states of blood oxygenation, blood flow, and oxidative metabolic rate can be described using the principle of conservation of mass or the Fick principle, which dictates that total oxygen is conserved. The relationship between resting (*rest*) and active (*act*) flow (F), blood oxygenation in arteries (Q_a) and veins (Q_v), and tissue oxygen consumption (Q'), is given as:

$$F_{rest}(Q_{a_{rest}} - Q_{v_{rest}}) - Q'_{rest} = F_{act}(Q_{a_{act}} - Q_{v_{act}}) - Q'_{act} \quad (2)$$

During activation, a 5% increase in oxidative metabolic rate has been reported [48]. While it is possible that this increase may affect the MR signal in several subtle ways, it is considered to be negligible in these simulations ($Q'_{rest} \approx Q'_{act}$). Equation (2) therefore reduces to:

$$(Q_{a_{act}} - Q_{v_{act}})/(Q_{a_{rest}} - Q_{v_{rest}}) = F_{rest}/F_{act} . \quad (3)$$

This relationship demonstrates that an activation-induced increase in flow unaccompanied by an increase in oxidative metabolic rate decreases the arterial-venous oxygenation difference by increasing the venous oxygenation. This decrease in the arterial-venous blood oxygenation difference causes an average increase in blood oxygenation in the vicinity of the activated region.

The relationship between blood volume and blood flow is less clear. From the positron emission tomography (PET) literature, a coupling between flow and volume changes has been characterized in the context of hypercapnic stresses [52]. This relationship is given by:

$$V_{act}/V_{rest} = (F_{act}/F_{rest})^{0.5} . \quad (4)$$

Application of Equation (4) to activation-induced flow and volume changes requires that activation-induced changes follow similar mechanisms as those created as a result of hypercapnic stresses. Whether these mechanisms apply to the smaller and more localized activation-induced changes is unknown.

Fox et al. [48], using PET, measured an activation-induced increase in blood flow of about 30%, which using these relationships is associated with a change in venous $\%HbO_2$ from 60 to 65%. Using a bolus injection of Gd (DTPA) in conjunction with dynamic MRI [46], an average activation-induced blood volume change of $32 \pm 10\%$ was measured. This volume change is associated with an increase of flow of 75% and a change in venous oxygen saturation from 60 to 76%. In the models of Ogawa et al. [1] and Weisskoff et al. [3], activation-induced increases in blood flow of 70 and 75%, respectively were assumed. These changes correspond to an increase in venous blood oxygenation from a resting level of 60% to activated levels of about 73 and 74%, respectively.

From these literature values, it can be inferred that activation-induced increases in blood flow range from 30–70%. This range is quite large and may depend on many variables, which may include differences in the measurement methods and the type of brain activation. Also, the relationship between blood volume and blood flow is an estimate which also depends on many variables that may not be constant in all regions of activation and between subjects.

We also characterized the effect of blood oxygenation and blood volume changes on the MR signal. Keeping all other parameters constant, blood volume and oxygenation were varied over a wide range. The effect of flow changes, in themselves, on MR signal were not explicitly studied. The nonsusceptibility-related flow effects on MR signal have been extensively modeled elsewhere [53–56] and empirically characterized [53, 56–60]. Also, when using a $TR \geq 1$ s, nonsusceptibility-related MR signal changes related to flow changes are minimal relative to susceptibility-related signal changes [58].

When simulating the dependence of MR signal on parameters other than blood oxygenation and volume, we kept blood oxygenation and volume fixed at 60% (assumed venous oxygen saturation) and 4%, respectively, or we assumed an activation-induced venous oxygen saturation change from 60% (resting) to 75% (active). Activation-induced changes in blood volume were not considered in most of the simulations (i.e., a constant volume of 4% was assumed), but a demon-

stration of the relative effects that a combined increase in blood volume and oxygenation have on the MR signal is given. In general, it is shown that the activation-induced increases in blood oxygenation greatly outweigh the effect from an increase in blood volume.

Other hemodynamic changes that may be significant and are not simulated directly include activation-induced changes in blood flow velocity, proton exchange rate, and hematocrit.

C. Biophysical Considerations. The relationship between the nuclei procession frequency and the applied magnetic field is given by:

$$\omega_o = \gamma B_o \tag{5}$$

where ω_o is the Larmor (or precession) frequency in rads per second. The value γ is the gyromagnetic ratio (267.5×10^6 rad/T for protons). The value B_o is the strength of the applied magnetic field (Tesla). If, within a voxel, the magnetic field is perturbed (i.e., by an object having a susceptibility not equal to the surrounding medium), a distribution of B_o will be present. The spins will therefore precess at different frequencies and lose coherence (dephase), generally causing a loss of signal. As will be described in more detail, this dephasing depends on several other factors, including the dynamics of the spins in the vicinity of the field perturber, the geometry of the perturber, and the magnetic susceptibility ($\Delta\chi$) of the perturber.

In the following section, the relationship between blood oxygenation and spin precession frequencies within the vicinity of a vessel containing whole blood is described. First, the relationship between blood oxygenation and resonance frequency independent of vessel geometry is considered. Second, geometrical considerations are included.

Weisskoff et al. [11] measured the volume susceptibility difference between fully deoxygenated blood and fully oxygenated red blood cells to be 0.18×10^{-6} (cgs units). To obtain the bulk susceptibility of whole blood (blood cells and plasma), it is necessary to multiply this number (applicable to red blood cells) by the volume fraction of red blood cells in the vasculature. Considering a hematocrit of 42, the susceptibility difference between fully oxygenated and fully deoxygenated whole blood is 0.756×10^{-7}.

Neglecting geometry at this point, the relationship between the frequency offset and the oxygenation of red blood cells is:

$$\Delta\omega = 2\pi\omega_o \, \Delta\chi(1 - Y) \tag{6}$$

where Y is the fractional blood oxygen saturation and $\Delta\chi$ is the susceptibility difference between fully deoxygenated red blood cells and surrounding plasma. As a reasonable approximation, the susceptibility of fully oxygenated blood cells and surrounding plasma is considered to be equal. When considering whole blood effects (i.e., the frequency offset induced by a vessel containing blood), it is necessary to multiply the fully deoxygenated red blood cell $\Delta\chi$ by the fraction of red blood cells in the vessel (i.e., hematocrit/100). Equation (6) can also be considered to describe the frequency offset induced at the surface of an infinite cylinder having a susceptibility difference $\Delta\chi$ and oriented perpendicularly to B_o.

An infinite cylinder having susceptibility difference $\Delta\chi$ that is placed in a magnetic field causes B_o distortions that are highly dependent on the orientation of the cylinder and location in space relative to the cylinder. The geometric relationships of the cylinder are illustrated in Figure 1. The spatial dependence of the induced frequency offset, $\Delta\omega$, on the orientation of the vessel (infinite cylinder) relative to the direction of B_o is given below [1, 61]. The variable $\Delta\omega'$ is equal to $\Delta\omega$, given in Equation (6).

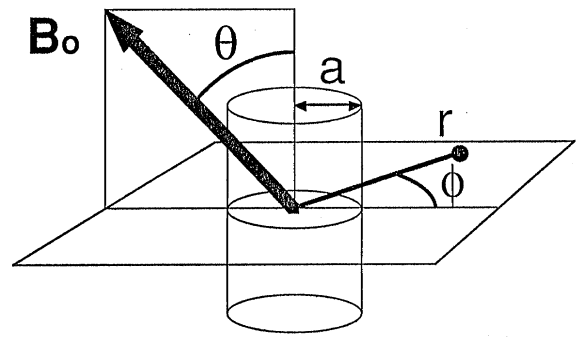

Figure 1. The geometrical relationships that determine resonant frequency shifts in the vicinity of an infinite cylinder placed in a magnetic field, B_o.

$$\text{Outside cylinder: } \Delta\omega(r, \theta, \phi) = \Delta\omega' \sin^2(\theta)(a/r)^2 \cos(2\phi) \tag{7}$$

$$\text{Inside cylinder: } \Delta\omega(\theta) = \Delta\omega'[3\cos^2(\theta) - 1]/3 \tag{8}$$

The angle of the cylinder axis relative to B_o is θ. The radius of the cylinder is a, and the distance from the center of the cylinder to the point of interest along a plane perpendicular to the cylinder is r. The angle between the vector, r, and the component of B_o on the perpendicular plane is ϕ.

Because the magnetic field does not vary along the length of the cylinder, these dephasing effects can be simulated in two dimensions. A subvoxel cell, as described subsequently, was used. In this cell we used one cylinder at a time, having a random θ distribution between 0 and $\pi/2$, and then carried out the complex addition of the magnetization in each cell in each time increment to compute the degree of dephasing. The effect of overlapping fields was not considered here.

The net phase shift created between intravascular spins and extravascular spins was taken into consideration. Intravascular dephasing as a result of susceptibility differences between red blood cells and plasma was not considered here. The amount of intravascular signal can vary considerably, as the T_2 and T_2^* of blood at a given hematocrit and oxygenation varies with field strength. Models using Monte Carlo methods [6, 7, 9] and ongoing work using the method presented here consider this potentially significant intravascular dephasing effect.

In general, the significance regarding the effects on the relative magnitudes of the transverse relaxation rate changes of curved geometry, overlapping cylinders, intravascular effects, or heterogeneous spin dynamics is unclear. In later stages of modeling work, the significance of these parameters should be considered. It is necessary, though, first to construct a simplified model such that the most basic relationships can be understood. This model was formulated as a first step to aid in the clarification of fundamental relationships between basic parameters (which are modulated) and relative gradient-echo and spin-echo dephasing effects.

III. DETERMINISTIC "PHASE ROTATE" AND "SMOOTH" MODEL

In this section, details are given as to how the simulation parameters—diffusion coefficient, vessel radius, blood volume, blood oxygen saturation, field strength, and vessel orientation relative to B_o—were manipulated. Also, a description is given of the manner in which the effects of diffusing spins through microscopic magnetic field gradients are simulated.

A. Matrix Construct: Subvoxel Map Relationships. Computer modeling of diffusion effects has been performed with random walk simulations which track the positions of a group of spins over time and record their phase histories [1, 2, 4, 6, 8, 62, 63]. This requires the calculations of randomized trajectories for a large number of spins to arrive at a solution with high precision. In the simulations presented here, diffusion is simulated by convolving a spin density map with a smoothing function. This method, first introduced by Wong et al. [10], was the basis for our method of modeling diffusion effects.

At any instant in time, the state of the spins in a voxel can be described by maps of the magnetization at subvoxel resolution. If these maps are sufficiently fine so that they are smooth over the unit cell, then for the purposes of the MR signal they completely define the state of the spins in that voxel, and it is not necessary to track the phase history of individual spins. In every unit of time, dt, the effects of diffusion and susceptibility can be described by a smoothing function (i.e., a Gaussian distribution) and a spatially dependent phase rotation (i.e., by a rotation matrix derived by the $\Delta\omega$ map), respectively. If dt is small enough so that the distance spins move due to diffusion is small relative to the scale of the field inhomogeneities, then this will be a good approximation of the simultaneous diffusion and dephasing process. It was determined that a dt of 1 ms was a sufficiently small time interval such that, in the range of geometries, susceptibilities, and diffusion coefficients common to the cerebral vasculature, the error due to quantization of time was $<1\%$ [10].

To simulate diffusion in the presence of a field perturber, three two-dimensional (128×128) subvoxel maps were created. The first map is of complex magnetization. At time = 0, this map is real and uniformly one. The second map is the frequency offset of $\Delta\omega$ and is converted into a map of the corresponding rotation matrices for one time interval, dt. The third map is a probability distribution map for diffusing spins in the span of one time interval, dt. As will be demonstrated, the magnetization map is "phase rotated" and "smoothed" in 1-ms intervals. In each 1-ms step, the magnetization of each voxel evolves in the presence of a specific $\Delta\omega$, and then is smoothed by the probability function. The methods by which these two maps are created and used are described subsequently.

Figure 2 shows the relevant variables in the creation of the $\Delta\omega$ map and the Gaussian map. Figure 2a shows the relationships that determine the radius of the capillary relative to the matrix size. Because the map is two-dimensional, the fractional blood volume is proportional to the area of the capillary relative to the area of the entire map. Figure 2b is the Gaussian probability distribution for a randomly diffusing spin over time interval dt. As described by Le Bihan et al. [24], the probability that a molecule travels a distance r during a time interval t can be described, in the case of a simple liquid, by a Gaussian distribution with zero mean. The mean squared path of the diffusing molecule (also the variance of the distance traveled), $\langle r^2 \rangle$, is proportional to the time interval, t, according to the Einstein equation, which, in three dimensions, is:

$$6Dt = \langle r^2 \rangle \tag{9}$$

where D is the diffusion coefficient. Because magnetization

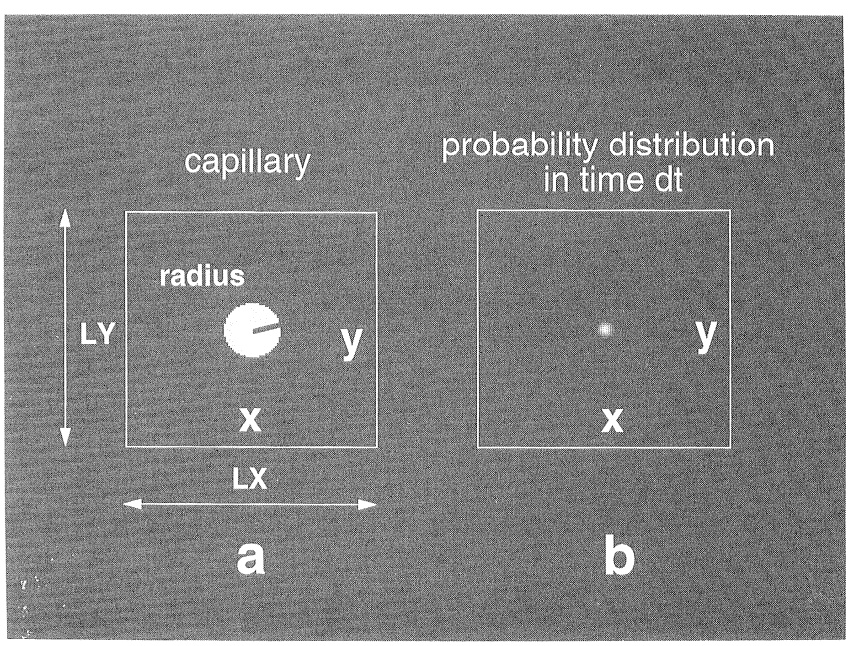

Figure 2. Parameters relevant to the subvoxel matrices in the simulations: (a) the capillary matrix; (b) the probability distribution matrix.

does not vary parallel to an infinite cylinder axis, the projection of Equation (9) onto two dimensions is considered in the simulation. The projection of the mean squared path onto a two-dimensional plane is given by:

$$4Dt = \langle r^2 \rangle \,. \tag{10}$$

The next step is to derive the relationship between the standard deviation, σ, of the Gaussian distribution used in the simulation and the physical parameter that is considered (i.e., the diffusion coefficient, D). A Gaussian distribution function, $f(r)$, with mean = 0 and standard deviation = σ, is given below [64]:

$$f(r) = \frac{1}{\sqrt{2\pi\sigma}} e^{\left(\frac{-r^2}{2\sigma^2}\right)} \tag{11}$$

The mean squared path of a freely diffusing spin, $\langle r^2 \rangle$, is equal to the expectation value of r^2 in a Gaussian probability distribution. This expectation value is obtained by integration of the Gaussian times r^2 over all space, then by dividing by the integral of the Gaussian only, over all space:

$$4Dt = \langle r^2 \rangle = \frac{\int_0^\infty r^2 \left(\frac{1}{\sqrt{2\pi\sigma}} e^{\left(\frac{-r^2}{2\sigma^2}\right)} \right) r\, dr}{\int_0^\infty \left(\frac{1}{\sqrt{2\pi\sigma}} e^{\left(\frac{-r^2}{2\sigma^2}\right)} \right) r\, dr} \,. \tag{12}$$

Equation (12) reduces to:

$$4Dt = \langle r^2 \rangle = 2\sigma^2 \,. \tag{13}$$

The relation between the standard deviation of the Gaussian, σ, and D is given by:

$$\sigma = \sqrt{2Dt} \tag{14}$$

where t is equal to dt, the time increment used in the simulations. The probability function, after normalization to the matrix dimensions is:

$$\text{prob}(x, y) = \left(\frac{LX \times LY}{2\pi} \right) \frac{1}{\sigma^2} e^{-\left(\frac{x^2+y^2}{2\sigma^2}\right)} \tag{15}$$

where LX and LY are the probability density matrix dimensions, and x and y are the coordinates within the matrix.

At this point, it is instructive to give several examples of the dependence of the $\Delta\omega$ maps and the Gaussian maps on the parameters that can be manipulated. Figures 3–8 show how the $\Delta\omega$ maps and the Gaussian maps vary with: a) diffusion coefficient; b) vessel radius; c) fractional blood volume; d) fractional blood oxygen saturation; e) magnetic field strength, B_o; and f) the angle between the cylinder axis and the B_o vector. In each example, the parameters that are held constant are given at the bottom of each figure.

Figure 3 gives an example of how the Gaussian probability density map changes when the diffusion coefficient is varied. The $\Delta\omega$ map remains the same but the width, in pixels, of the Gaussian is increased as D increases from 1 to 20 $\mu m^2/ms$.

Figure 4 gives an example of how the Gaussian map changes when the vessel radius is varied. The $\Delta\omega$ map again remains the same but the width, in pixels, of the Gaussian is decreased as the radius is increased from 2.5 to 20 μm.

Figure 5 gives an example of how both the Gaussian and $\Delta\omega$ maps change when the fractional blood volume is varied: The vessel radius, in submatrix pixels, is increased (because the area is proportional to the blood volume) and the width of the Gaussian increases accordingly to match the width of the simulated vessel (so that the diffusion distance relative to the vessel radius is kept constant). Here, the blood volume fraction is varied from 2–20%.

Figure 6 gives an example of how the $\Delta\omega$ map changes when the fractional blood oxygen saturation is varied. When whole blood becomes less saturated, the frequency offsets in

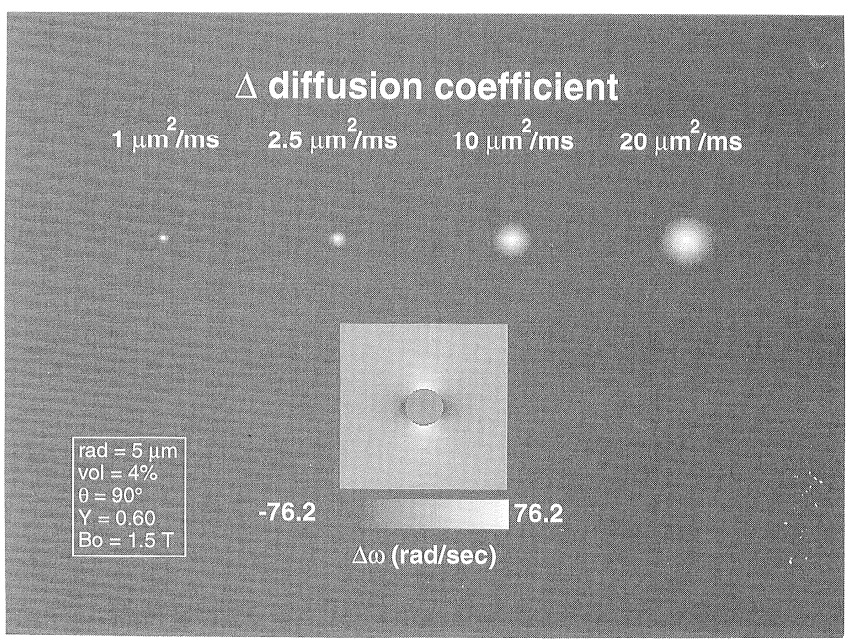

Figure 3. Example of the manner in which the Gaussian map changes when the diffusion coefficient is varied.

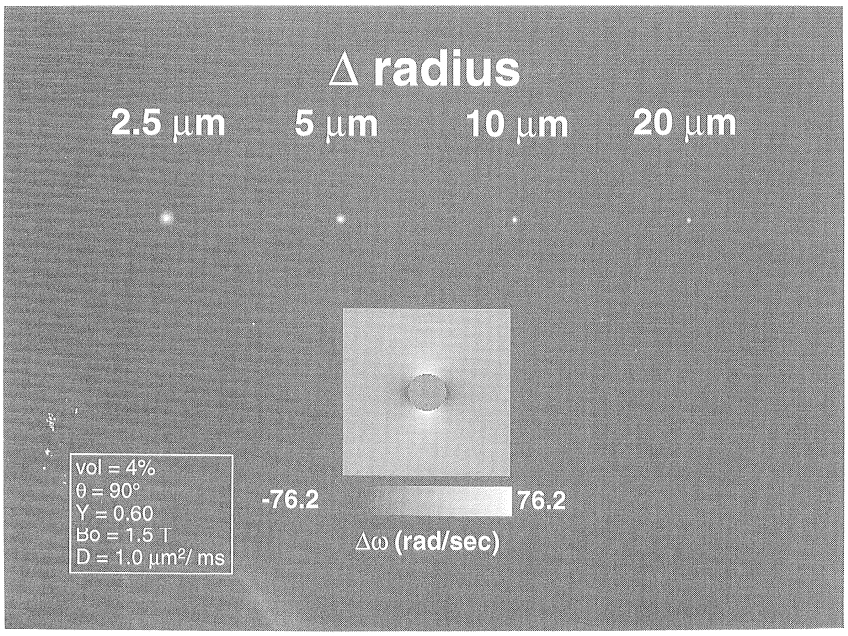

Figure 4. Example of the manner in which the Gaussian map changes when the vessel radius is varied.

the vicinity of the cylinder are increased. Here, the blood oxygen saturation is varied from 90 to 0%.

Figure 7 gives an example of how the $\Delta\omega$ map changes when the magnetic field strength, B_o, is varied. When the field strength is increased, the frequency offsets in the vicinity of the cylinder are increased. Here, the field strength is varied from 0.5–4.0 T.

Finally, Figure 8 shows an example of how the $\Delta\omega$ map changes when the angle, θ, between the cylinder axis and the direction of B_o is varied. The field distortions (frequency offsets around the cylinder) are nonexistent when the cylinder is parallel to B_o. Here, the angle, θ, is varied from 0° (parallel) to 90° (perpendicular).

These basic examples illustrate the relationships that were created to simulate susceptibility effects in the presence of diffusing spins. In the next section, the details of the simulation process are described.

B. Diffusion Simulation Methodology. At time zero, we placed uniform and coherent transverse magnetization across the matrix. With each "phase rotate" and "smooth" iteration, every subvoxel in the matrix accumulated a particular real and

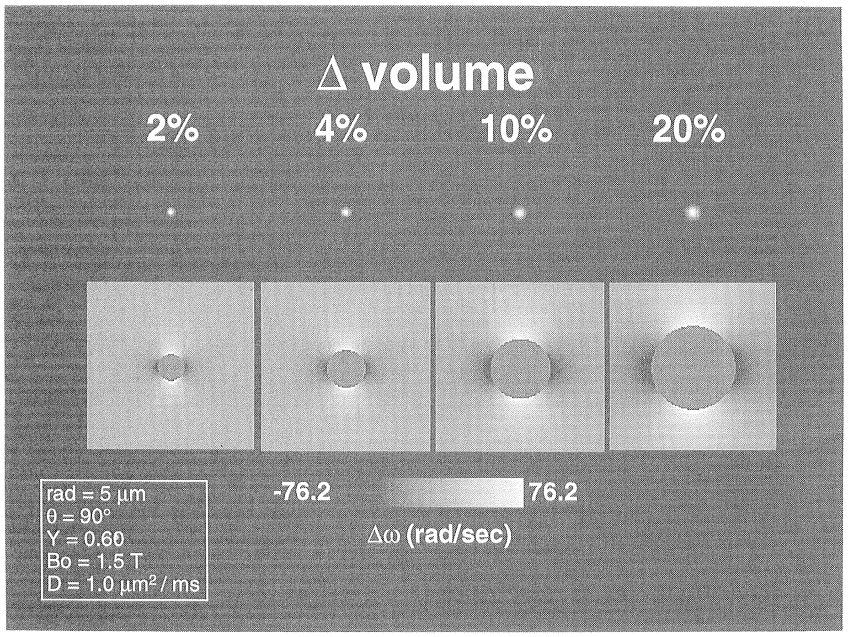

Figure 5. Example of the manner in which the $\Delta\omega$ and Gaussian maps change when the fractional blood volume is varied.

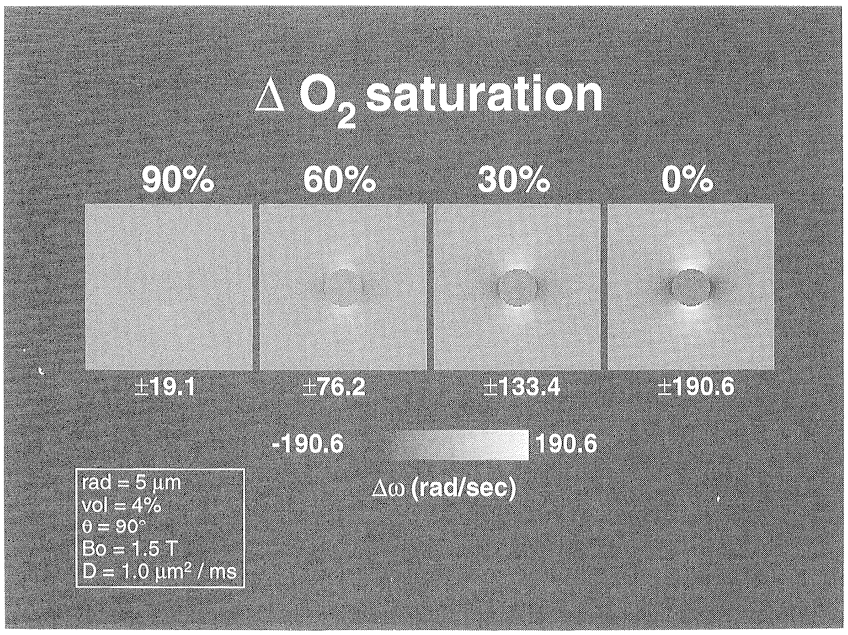

Figure 6. Example of the manner in which the $\Delta\omega$ map changes when the fractional blood oxygen saturation is varied.

imaginary component. This iteration process is illustrated schematically in Figure 9. To simulate a 180° RF pulse, as would be applied for a spin-echo sequence, the imaginary component of the magnetization was multiplied by -1 at time = TE/2.

An example is given to demonstrate the simulation process. In this example, a single cylinder oriented perpendicularly to B_o is used. The echo time of the experiment is 60 ms. The vessel radius is 10 μm, the diffusion coefficient is 1 μm^2/ms, and the field strength is 1.5 T. The blood oxygenation saturation is 0.6, and the hematocrit is 42. Figures 10 and 11 show the time evolution of the magnetization during gradient-echo and spin-echo sequences respectively. Real (i), imaginary (q), and magnitude (m) maps evolve in time from left to right. Ten iterations take place between each box. In the gradient-echo simulation, the imaginary component begins to resemble a blurred version of the frequency offset map ($\Delta\omega$) used in this simulation. Signal (m) dropout is observed as a result of subvoxel dephasing over time.

In the spin-echo map, the sign of the imaginary component map is reversed immediately prior to the 30-ms maps. After the application of the 180° pulse, the phase is reversed. If no

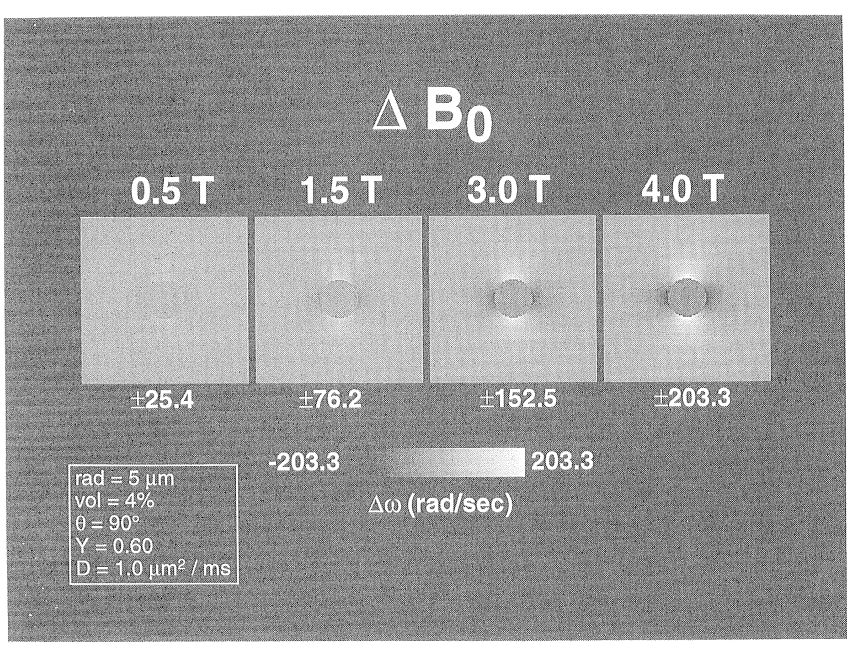

Figure 7. Example of the manner in which the $\Delta\omega$ map changes when the magnetic field strength, B_o, is varied.

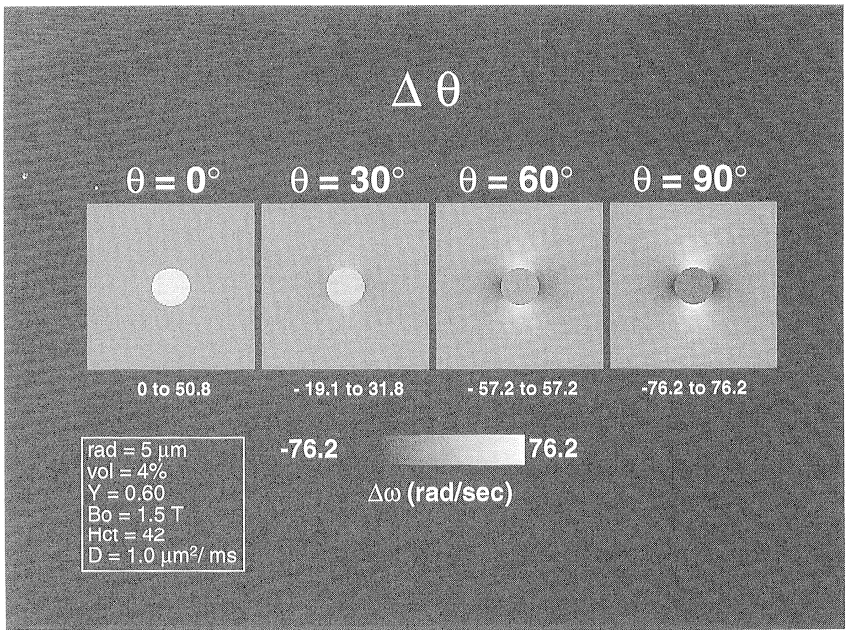

Figure 8. Example of the manner in which the $\Delta\omega$ map changes when the angle, θ, between the cylinder axis and B_o is varied.

diffusion were to occur, both the real and imaginary components would return to maps of 1s and 0s, respectively, at the echo time, TE. However, the signal does not completely recover because the diffusion processes causes spins to experience different B_o fields in different locations before and after the 180° pulse.

Figure 12 demonstrates the evolution of the signal intensity over time for the spin-echo and gradient-echo sequences. The signal intensity at each time point is calculated by complex addition of the magnitude.

IV. SIMULATIONS

The goal in these simulations was to characterize the dependencies of ΔR_2^* and ΔR_2 on relevant physiologic and biophysical variables. An understanding of these dependencies

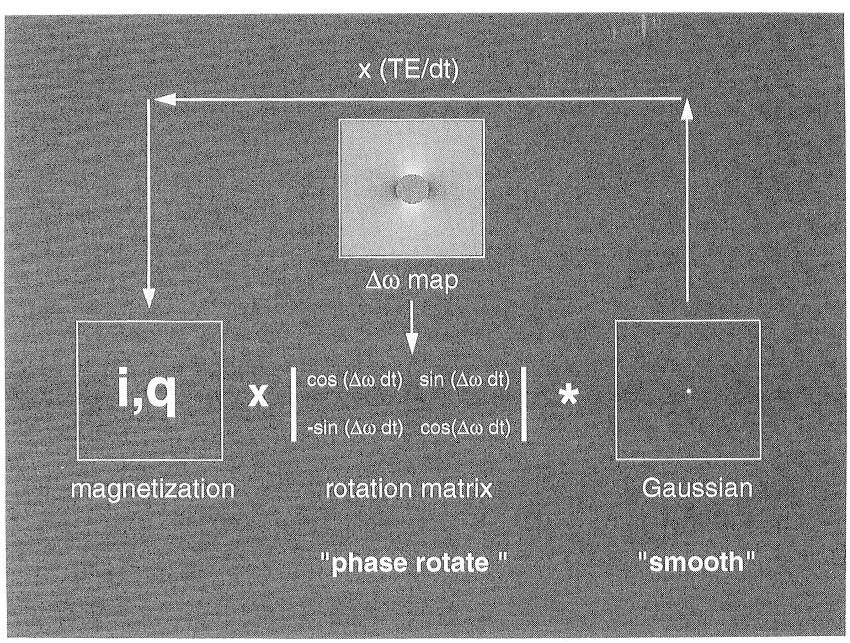

Figure 9. The basic methodology of the simulation involves an iterative process by which the magnetization map is multiplied by the frequency offset map and subsequently convolved with the Gaussian map. The iteration step, *dt*, is 1 ms in this simulation.

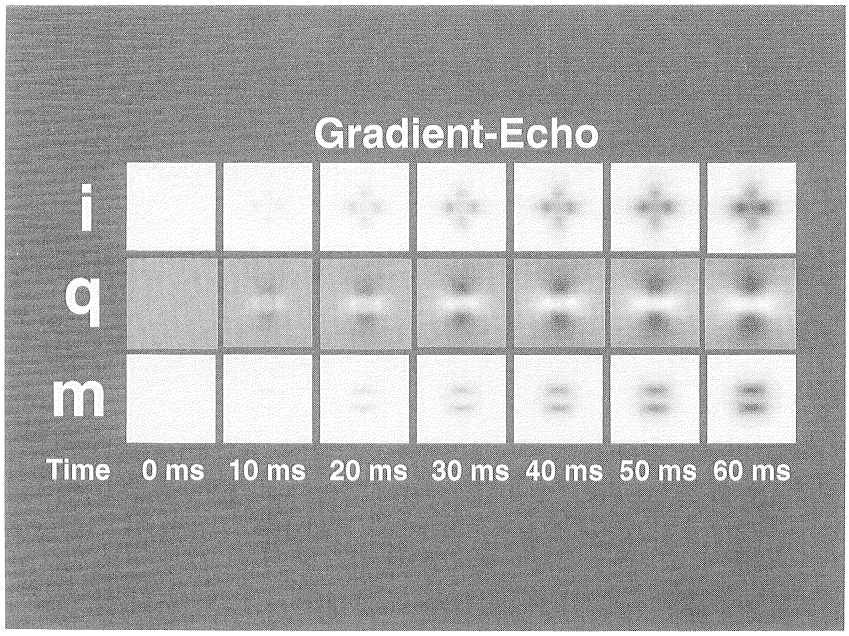

Figure 10. Gradient-echo simulation. The time evolution of the real (i), imaginary (q), and magnitude (m) components of the magnetization as they evolve during the iterative phase rotation and smoothing process.

may allow more accurate interpretation of activation-induced signal changes. This section includes basic simulations, model validation, a demonstration of ΔR_2^* and ΔR_2 dependence on $\Delta\omega$ and τ, and ΔR_2^* and ΔR_2 dependence on physiologic parameters.

A. Basic Simulations. It is instructive to provide a demonstration of the relative (spin-echo to gradient-echo) signal changes that occur if only the vessel radius is varied. Three signal vs. time plots for each pulse sequence corresponding to vessel radii of 2.5, 5, and 20 μm are shown in Figure 13a and b.

With the spin-echo sequence, the signal intensity remained high for the smaller vessel, then dropped for the intermediate-size vessel, and increased when the vessel size was increased to 20 μm. For the smallest vessel, the overall spin coherence

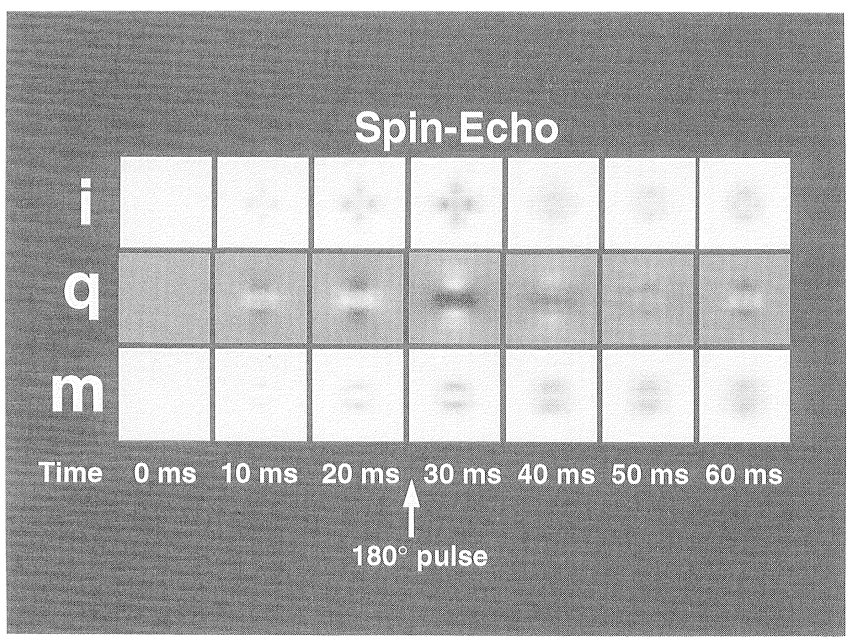

Figure 11. Spin-echo simulation. The time evolution of the real (i), imaginary (q), and magnitude (m) components of the magnetization as they evolve during the iterative rotation and smoothing process. The 180° pulse reverses the sign of the imaginary component, but because of the diffusion process, the spins are not completely refocussed at the echo time *TE*.

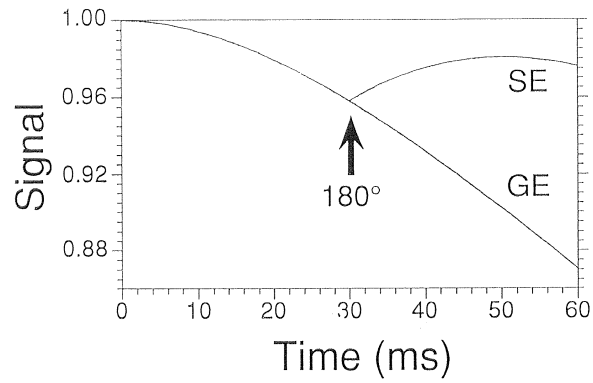

Figure 12. Corresponding plots of signal vs. time for the simulated spin-echo and gradient-echo sequences, corresponding to the maps in Figures 10 and 11. The 180° RF pulse is applied for the spin-echo sequence.

remained high as a result of the relatively rapid diffusion-mediated averaging of field offsets contained in the small region around the 2.5-μm vessel. At the other extreme (20-μm-size vessel), the diffusion effects were minimal because of the relatively large region that the field offset covered relative to the diffusion distance. In this case, the 180° pulse almost completely reversed the dephasing effects created by the large vessel; and thus, the diffusional averaging was minimal.

With the gradient-echo sequence, the signal intensity decreased monotonically as the vessel size increased. Diffusional averaging of the field gradients, which maintained spin coherence, decreased as the size of the perturber increased. A 180° pulse was not applied; therefore, the spin phase was not reversed.

As the vessel size approaches infinity, the diffusion effects approach zero. In this case, the spin-echo sequence shows complete recovery of signal at the echo time, TE, and the gradient-echo sequence is maximally dephased, having no motional averaging effects which tend to maintain spin coherence.

The relative effects of perturber size, frequency offset, and diffusion coefficient on relative spin-echo and gradient-echo signals has been categorized roughly into "exchange regimes." This description, given in Table I, is an approximation based on spherical geometry, but is also useful when discussing cylindrical geometry. When the radius, R, equals 20 μm and

Table I. Exchange regimes commonly referred to when describing the effects of magnetic field perturbations on transverse relaxation rates.

Slow exchange	$\tau(\delta\omega) \gg 1$	$\Delta R_2^* \gg \Delta R_2$ $\Delta R_2' \approx \Delta R_2^*$
Intermediate exchange	$\tau(\delta\omega) \approx 1$	$\Delta R_2^* > \Delta R_2$ $\Delta R_2' < \Delta R_2^*$
Fast exchange	$\tau(\delta\omega) < 1$	$\Delta R_2^* \approx \Delta R_2$ $\Delta R_2' \approx 0$

D equals 1 $\mu m^2/ms$, the frequency offset at the surface of the vessel, $\Delta\omega$, equals 76.2 rad/s, (i.e., $\%HbO_2 = 60\%$, $B_o = 1.5\ T$; hematocrit = 42, considering that $\Delta\chi$ of completely deoxygenated blood cells equals 0.18×10^{-6}); and $\Delta\omega(R^2/D) = 30.5$. In this "slow exchange" or "linear gradient" regime, spin-echo signal showed much less attenuation than gradient-echo signal, as is demonstrated in Figure 13.

When the vessel radius was changed to 5 μm, (all other parameters remaining the same), $\Delta\omega(R^2/D) = 1.90$. In this "intermediate exchange" regime, both the spin-echo signal and gradient-echo signal showed less attenuation overall.

Finally, when the vessel radius was changed to 2.5 μm (all other parameters remaining the same), $\Delta\omega(R^2/D) = 0.476$. In this "fast exchange" or "motionally averaged" regime, both the spin-echo and gradient-echo signals showed the least attenuation overall.

To apply these effects to activation-induced signal changes caused by a change in $\Delta\chi$, the simulation was performed at two different blood oxygenation saturation values: 0.60 and 0.75. The relative changes in signal corresponding to a change in blood oxygenation from 0.60 to 0.75 are shown in Figure 14.

If the assumption is made that the source of the signal change is due to the transverse relaxation rate that can be modeled as a single exponential, then the relationship between signal and relaxation rate is:

$$-Ln(Sa/Sr)/TE = \Delta R_2(^*)\,. \tag{16}$$

where Sa and Sr are the active and resting state MR signal intensities. $\Delta R_2(^*)$ stands for either ΔR_2 or ΔR_2^*. This is a more general manner of describing the relative spin-echo and gradient-echo signal changes, because, given a relaxation rate change, the percent signal change will increase with TE. The relationship between the percent signal at a given TE and $\Delta R_2(^*)$ is:

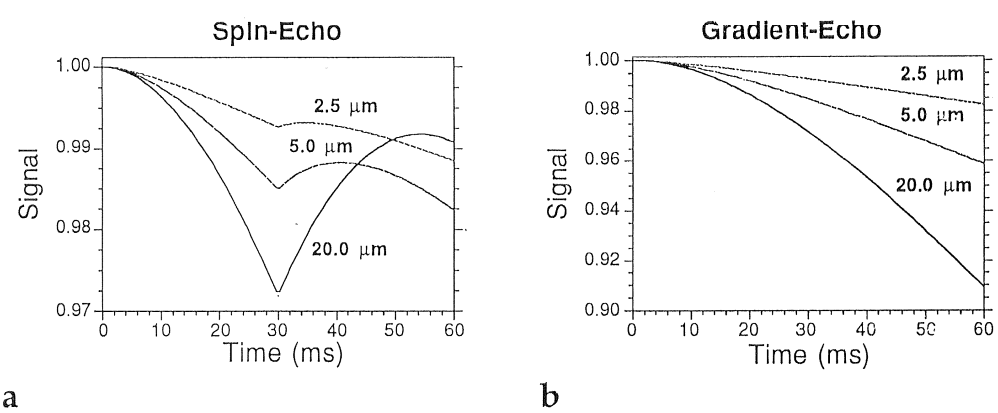

Figure 13. The effect of changing the perturber radius on: (a) spin-echo and (b) gradient-echo signal.

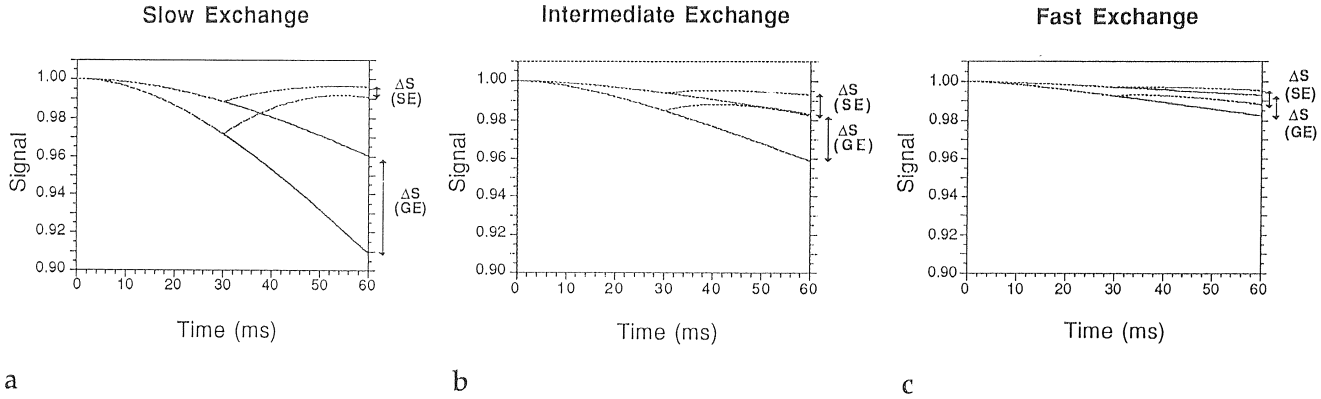

Figure 14. (a) Example of signal evolution for spin-echo (SE) and gradient-echo (GE) sequences when the perturber of radius: (a) 20 μm; (b) 5 μm; and (c) 2.5 μm has $\Delta\chi$ altered in a manner corresponding to an activation-induced blood oxygen saturation change from 0.60 to 0.75.

$$\text{Percent signal change} = 100(e^{-\Delta R_2^* TE} - 1)\,. \qquad (17)$$

The fractional signal change increases in an approximately linear manner with TE, but the signal difference reaches a maximum at $TE \approx T_2(^*)$. It is for this reason that most FMRI studies are performed at $TE \approx T_2(^*)$.

In all simulations, the active (Sa) and resting (Sr) signals were obtained at a TE of 60 ms. The signal change was then converted to ΔR_2^* and ΔR_2 by the use of Equation (16). It was determined that the fairest spin-echo to gradient-echo comparison would be at TE values which were the same and within the range typically used experimentally. Therefore, a TE of 60 ms was chosen.

The $\Delta R_2^*/\Delta R_2$ ratios from this example increased from 1.53 (fast exchange) to 2.38 (intermediate exchange), to 9.98 (slow exchange). Figure 15 complements the results obtained in Figure 14. The frequency offset map is shown on the upper left, and the Gaussian probability distributions relative to the field map for each radius are shown on the right.

B. Model Validation. As a validation of the model methodology, a direct comparison was made with results obtained from the Monte-Carlo simulation method of Ogawa et al. [1]. We made two specific comparisons. First, a comparison was made with the study of the off-resonant frequency dependence of ΔR_2^* shown in Figure 3 from Ogawa et al. [1]. Second, a comparison was made with the study of spin-echo

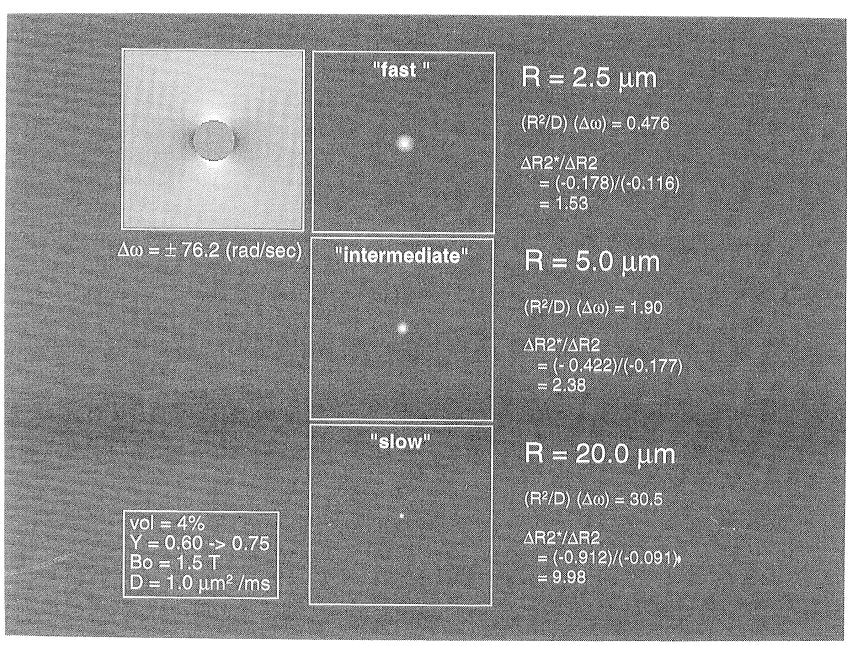

Figure 15. Summary of the magnetization map and the Gaussian distributions used for the signal decay plots shown in Figure 14. At $(R^2/D)\Delta\omega = 0.476$ ("fast"), $\Delta R_2^*/\Delta R_2 = (-0.178/-0.116) = 1.53$. At $(R^2/D)\Delta_\omega = 1.9$ ("intermediate") $\Delta R_2^*/\Delta R_2 = (-0.422/-0.177) = 2.38$. At $(R^2/D)\Delta\omega = 30.5$, $\Delta R_2^*/\Delta R_2 = (-0.912/-0.0091) = 9.98$.

to gradient-echo fractional signal change ratio dependence on vessel radius that is shown in Figure 6 from Ogawa et al.

For comparison, the parameters and units were matched to the studies presented in the work of Ogawa et al. [1]. In the first comparison, ΔR_2^* was measured at five different $\Delta\nu$ (Hz) values. The perturber radius was set to 2.5 μm. The diffusion coefficient used was either zero or 1 $\mu m^2/ms$ (free diffusion). The blood volume fraction used was 2%. The value of ΔR_2^* was obtained by setting $Sa = 1$ and $Sr =$ the signal intensity obtained from the simulation. The results of the deterministic ("phase rotate" and "smooth") simulation are shown in Figure 16a, which demonstrates that with $D = 0$, the change in ΔR_2^* was linear with $\Delta\nu$. In the case that $D = 1\ \mu m^2/ms$, the dependence of ΔR_2^* on $\Delta\nu$ is greater than linear (approximately $B_o^{1.9}$). Both the shapes of the $D = 0$ and free diffusion $D = 1\ \mu m^2/ms$ curves and the actual values of ΔR_2^* match the results shown in Figure 3 of [1].

In the second comparison, using the deterministic model, we measured the relative fractional signal attenuation between spin-echo and gradient-echo signal sequences (Figure 16b): $TE = 40$; fractional blood volume = 2%; $\Delta\nu = 40$ Hz; $D = 1\ \mu m^2/ms$. These results correspond closely to those shown in Figure 6 from [1].

In general, although comparisons do not validate the model for every circumstance, the close agreement demonstrated between the results using the deterministic method and the results of Ogawa et al. [1] is encouraging and serves as an approximate validation of the technique.

C. General ΔR_2^* and ΔR_2 Dependence on $\Delta\omega$ and τ. This section gives a general description of the dependence of ΔR_2^* and ΔR_2 on τ ($\tau = R^2/D$). However, instead of varying parameters related to $\Delta\omega$ (which include B_o, hematocrit, blood oxygenation, and $\Delta\chi$ of fully deoxygenated red blood cells), $\Delta\omega$ is varied directly. Also, instead of varying parameters related to τ (including R and D), τ is varied directly.

Figure 17 shows ΔR_2^* ($Sa = 1$, and $Sr =$ signal intensity at 60 ms) vs. $\Delta\omega$ over a range of R^2/D values. The vertical bands indicate the off-resonance frequency range that was covered when the oxygen saturation of whole blood changed from 0.60 (right edge of band) to 0.75 (left edge of band). At higher field strengths, the bands become progressively wider and ΔR_2^* also increases. These results illustrate that given the same oxygenation change, the activation-induced signal change will be greater at a higher field. The assumption was also made that the relative intravascular and extravascular baseline signal intensities were the same across field strengths. As R^2/D increased, ΔR_2^* became greater at a given $\Delta\omega$, but the slope of the curve was nearly linear, especially at high $\Delta\omega$ values.

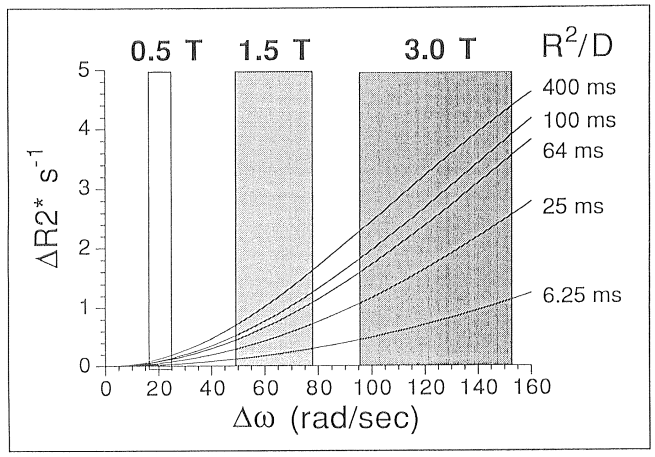

Figure 17. ΔR_2^* vs. $\Delta\omega$ at different values of τ (R^2/D). The increase in ΔR_2^* is monotonic with frequency and τ. The vertical bands indicate the maximum frequency shift at each field strength that corresponds to a change in hemoglobin saturation from 0.6 to 0.75.

Figure 18 similarly shows ΔR_2 vs. $\Delta\omega$ over a range of R^2/D values. At a given $\Delta\omega$, ΔR_2 was lowest at high R^2/D (slow exchange), then increased until a maximum was reached at $R^2/D = 25$ ms (intermediate exchange), then decreased again as R^2/D decreased further.

Figure 19 shows $\Delta R_2^*/\Delta R_2$ measured across $\Delta\omega$ and R^2/D. The ratios increased with increasing R^2/D. The ratios showed a relative insensitivity to $\Delta\omega$, which is in agreement with the reported ratios in the literature [20], demonstrating that the measured $\Delta R_2^*/\Delta R_2$ ratio is relatively field strength-insensitive.

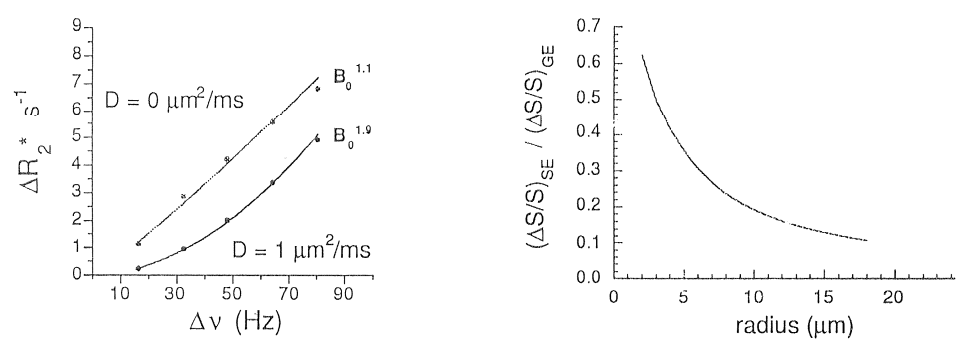

a b

Figure 16. Results from deterministic simulations that are directly compared with Monte Carlo simulations of Ogawa et al. [1]: (a) Comparison with Figure 3 of Ogawa et al. Demonstration of susceptibility-induced R_2^* change calculated in a voxel containing 2.5-μm blood vessels. (b) Comparison with Figure 6 of Ogawa et al. The ratio of $\Delta S/S$ for spin echo to $\Delta S/S$ for gradient echo signal as a function of cylinder radius (blood volume = 0.02, $TE = 40$ ms, $\Delta\nu = 40$ Hz).

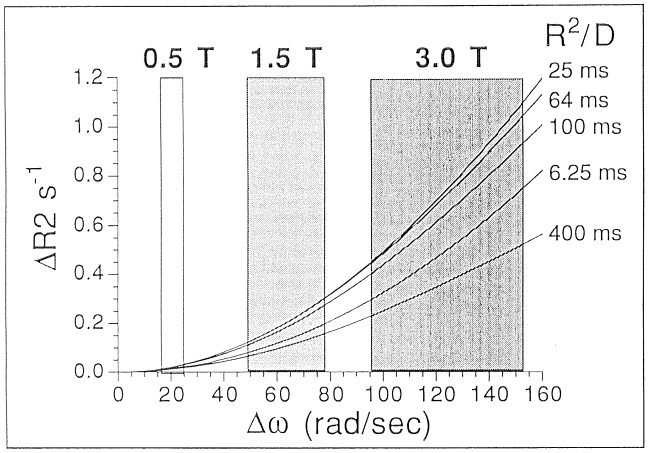

Figure 18. ΔR_2 vs $\Delta\omega$ at different values of τ (R^2/D). As τ was increased, ΔR_2 increased, reaching a peak at $\tau = 25$ ms, then decreased at higher τ values.

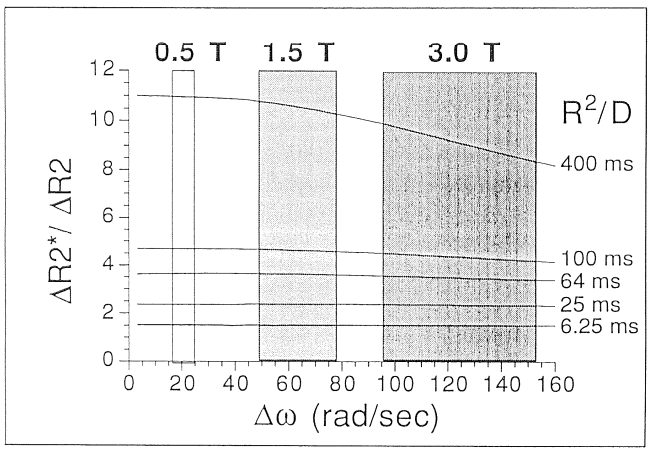

Figure 19. The $\Delta R_2^*/\Delta R_2$ demonstrating that the ratio is relatively insensitive to $\Delta\omega$.

D. ΔR_2^* and ΔR_2 Dependence on Physiologic Parameters. In this section, we modulated specific physiological parameters, one at a time. Specifically, we analyzed the absolute and relative ΔR_2^* and ΔR_2 changes that occur when: a) the vessel radius is varied across three field strengths; b) diffusion coefficient is varied; c) blood volume is varied; d) vessel orientation, relative to B_o, is varied; and e) blood oxygenation is varied. The parameters and their corresponding values, when not being modulated, are given in Table II.

Figure 20 shows the effects of varying the vessel radius from 2.5 to 20 μm at 0.5, 1.5, and 3 T. Figure 20a is of ΔR_2, and Figure 20b is of ΔR_2^*. The ΔR_2 values generally increased with field strength, but peaked at a vessel radius of about 6 μm at all field strengths. The ΔR_2^* values increased monotonically with vessel radius. These relaxation rate changes simulated across the entire range of radii and field strengths were comparable to those measured in active cortical regions [16, 17, 19–22, 58, 65].

Figure 21 shows the simulated $\Delta R_2^*/\Delta R_2$ ratios at all field strengths. As the vessel radius approached 0, the ratio approached 1 and both of the relaxation rate changes approached 0. This illustrates an important concept regarding endogenous susceptibility contrast. If the perturber size is too small and is homogeneously distributed, bulk susceptibility contrast will not exist. Other mechanisms not modeled here may still contribute. Only bulk susceptibility contrast of a compartmentalized field perturber that is large relative to the surrounding spin dynamics can account for the differences between ΔR_2^* and ΔR_2 that are consistently observed. The box in Figure 21 indicates the ratios typically measured experimentally at the three field strengths [16, 18–20, 58, 65]. The average compartment size (likely some combination of large vessels and intravascular red blood cell effects) is in the range of 7–12 μm.

Studies by Hoppel et al. [22] of $\Delta R_2^*/\Delta R_2$ on whole blood during changes in oxygenation reported a ratio of 1.5, which corresponds, in the simulated results, to a radius of 2.5 μm—about the radius of a red blood cell. These similarities to the whole blood data may be: a) incidental given the vastly different geometries, field overlap, and proton dynamics; or b) indicative that these geometric differences are not a large factor when considering dephasing in the fast exchange regime. More modeling studies, using this deterministic approach, of the effects of varying oxygenation on blood T_2^* and T_2 are currently being pursued to answer some of these questions and to complement modeling studies such as those of Gilles et al. [66] and experimental studies on whole blood such as those of Thulborn et al. [67] and Wright et al. [68].

Figure 22a shows the effect of the diffusion coefficient on ΔR_2^* and ΔR_2. Without diffusion, $\Delta R_2 = 0$ and ΔR_2^* was maximal for the $\Delta\omega$ and blood volume used. As the diffusion coefficient increased, the ΔR_2^* decreased and ΔR_2 first increased then decreased as D was increased further. Measured values of ΔR_2^* and ΔR_2 were comparable to the simulated values at $D = 0$–$5\ \mu m^2/ms$.

Figure 22b shows the $\Delta R_2^*/\Delta R_2$ ratio vs. D. Most experimentally obtained data lay in the elbow of the curve,

Table II. Constant variable values used: radius, field strength, diffusion coefficient, blood volume, angle, and blood oxygen saturation are modulated systematically.

Parameter	Value
Blood oxygen saturation	0.60 (resting) to 0.75 (active)
Vessel radius	10 μm
Blood volume	4%
$\Delta\chi$ of deoxygenated red blood cells	0.18×10^{-6} cgs
Vessel orientation	Random distribution
Diffusion coefficient	1 μm^2/ms (isotropic and unrestricted)
Field strength (B_o)	1.5 Tesla
Hematocrit	42

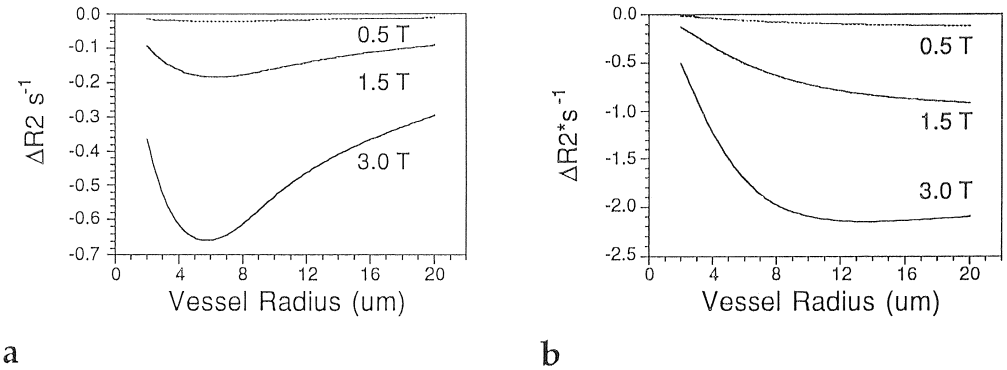

Figure 20. Effect of varying field strength on activation-induced changes in: (a) R_2 and (b) R_2^*.

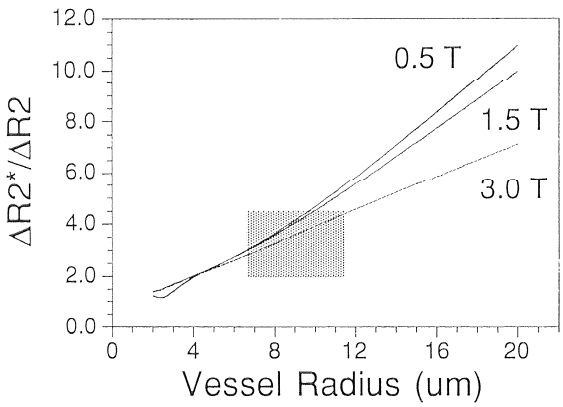

Figure 21. Ratio of ΔR_2^* (shown in Figure 6.25a) to ΔR_2 (shown in Figure 6.25b) at 0.5 T, 1.5 T, and 3.0 T. The box indicates the typical $\Delta R_2^*/\Delta R_2$ ratios reported in the literature.

where the diffusion coefficients were comparable to those found in the brain and in water. As D became large, the slope flattened considerably. The values and ratios simulated for diffusion coefficients $>5\ \mu m^2/ms$ may have been less accurate because of digitization errors when using a step size of 1 ms.

As mentioned, the blood volume may vary considerably from voxel to voxel. Figure 23a shows the simulated relaxation rate changes as they related to resting state blood volume. ΔR_2^* and ΔR_2 showed a strong dependence on blood volume. The ΔR_2^* and ΔR_2 values typically observed corresponded to blood volumes between 2 and 7%. Figure 23b shows the change in $\Delta R_2^*/\Delta R_2$ with volume change. Here, the ratio changed little.

In the brain and most likely in larger vessels, the predominant vessel orientation may vary considerably from voxel to voxel. The changes in relative relaxation rates that occurred with varying vessel angles are shown in Figure 24a. As described in Equations (7) and (8), and shown in Figure 8, the external gradients and intravascular frequency offsets varied considerably with angle. The values of ΔR_2^* and ΔR_2 appeared to be largest at 90°—the angle at which the surrounding gradients were largest. The effects were minimal at 45°—the angle in which the combined effect of the gradients and the internal frequency offset were minimal. The ΔR_2^* and ΔR_2 values appeared to increase as the angle was reduced to 0°—the angle at which the external gradients did not exist and the intravascular frequency offset was maximal.

The $\Delta R_2^*/\Delta R_2$ ratio change vs. angle is shown in Figure 24b. The ratio increased, then reached a plateau. This is likely related to the fact that the vessel was freely permeable and that the sharp $\Delta\omega$ difference (no gradient; just a step) that began to form in the immediate vicinity of the vessel wall (below 45°) contributed somewhat to spin-echo irreversible dephasing.

The resting blood oxygenation may vary considerably from

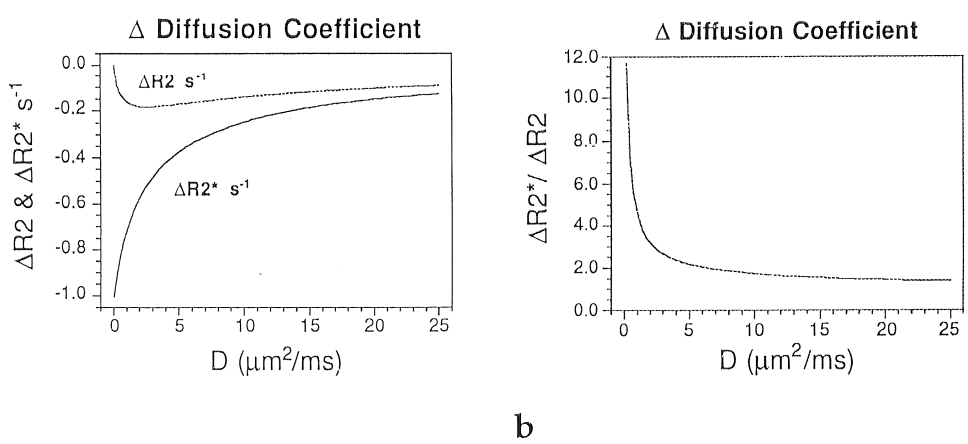

Figure 22. Effect of varying diffusion coefficient on activation-induced changes in R_2 and R_2^*: (a) R_2 and R_2^* vs. D. (b) $\Delta R_2^*/\Delta R_2$ vs. D.

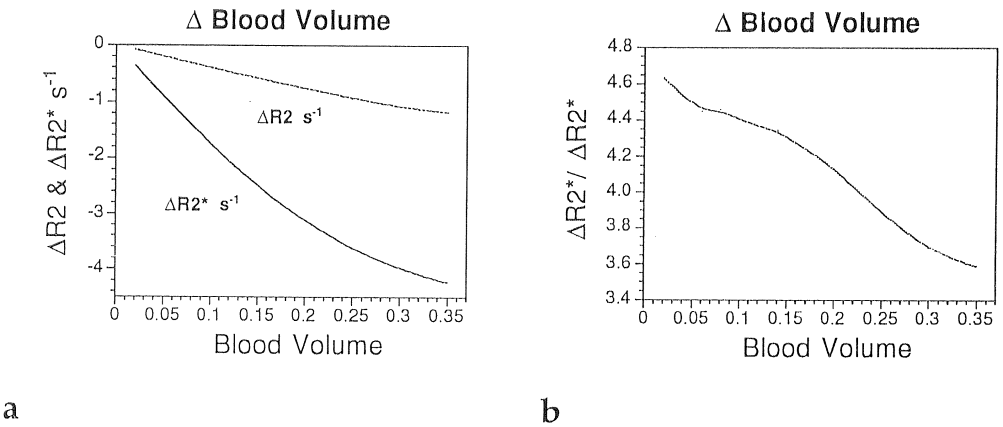

Figure 23. Effect of varying fractional blood volume on activation-induced changes in R_2 and R_2^*: (a) Relative R_2 and R_2^* vs. blood volume. (b) $\Delta R_2^*/\Delta R_2$ vs. blood volume.

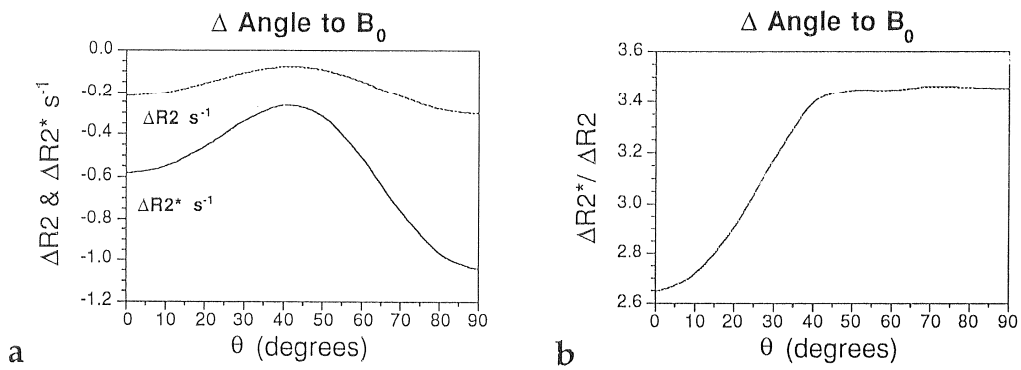

Figure 24. Effect of varying cylinder orientation relative to B_o on activation-induced changes in R_2 and R_2^*: (a) Relative R_2 and R_2^* vs. angle to B_o. (b) $\Delta R_2^*/\Delta R_2$ vs. angle to B_o.

voxel to voxel, along with the activation-induced blood oxygenation changes. If the slope of ΔR_2^* or ΔR_2 vs. $\%HbO_2$ changes, this may have a large effect on activation-induced signal changes. In the brain, the resting venous oxygen saturation is assumed to be 60%. The changes in ΔR_2^* and ΔR_2 that occurred as $\%HbO_2$ was increased to 75% were simulated. Figure 25a shows ΔR_2^* and ΔR_2 vs. $\%HbO_2$. Below 60% blood oxygenation, the slopes appeared to be

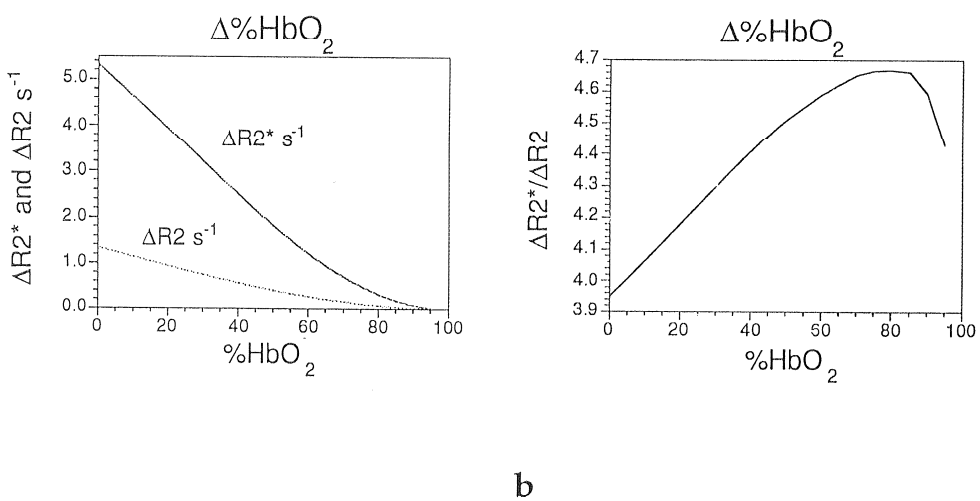

Figure 25. Effect of varying hemoglobin oxygen saturation on relative transverse relaxation rate: (a) Relative R_2 and R_2^* vs. $\%HbO_2$. (b) $\Delta R_2^*/\Delta R_2$ vs. $\%HbO_2$.

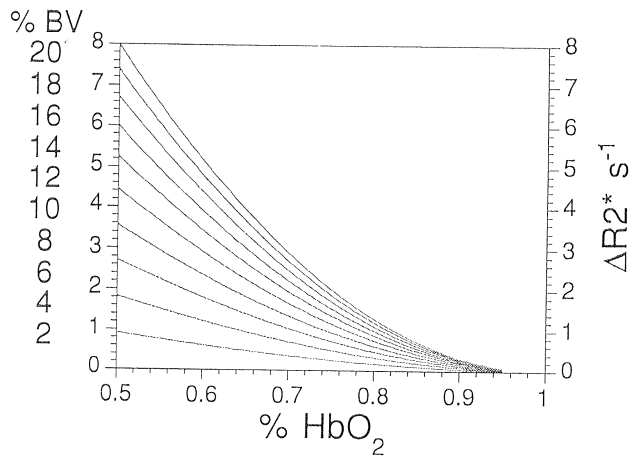

Figure 26. The relationship between blood oxygenation saturation and ΔR_2^* at different fractional blood volumes.

somewhat constant. Above a blood oxygen saturation of 60%, the slopes appeared to decrease. Figure 25b demonstrates that the $\Delta R_2^*/\Delta R_2$ ratio was not strongly sensitive to $\%HbO_2$.

E. Blood Oxygenation Changes vs. Blood Volume Changes. This section demonstrates that the concomitant activation-induced change in blood volume contributes much less significantly to the overall signal change than does the change in blood oxygen saturation. A common question that is asked in regard to the activation-induced MR signal change is: "Given constant oxygenation and an increase in volume, the MR signal drops, but given a constant blood volume and an increase in oxygenation, the MR signal increases. As both hemodynamic events happen during activation, which effect dominates?" To answer this question, it is necessary to determine the effects of simultaneous changes in blood volume and oxygenation.

Figure 26 shows $\%HbO_2$ vs. ΔR_2^*, similar to Figure 25a but having one curve for each blood volume ranging from 2–20%, as shown to the left. These figures most closely resemble the physiologic process of vessel recruitment, because the vessel radii are not varied when the volume is increased. Figure 26 shows the simultaneous relationship between blood volume and blood oxygenation. At the lowest oxygenation, a blood volume increase of an order of magnitude caused a change in ΔR_2^* of $8\,s^{-1}$. At the highest blood volume, a similar change in ΔR_2^* was caused only by decreasing the $\%HbO_2$ by 50%.

Using the physiologic relationships in Equations (3) and (4), we determined that with an activation-induced increase in flow (69% increase), the venous blood oxygen saturation would increase from 60 to 75%, and the blood volume would increase from 4 to 5.2%. Figure 27 demonstrates ΔR_2^* vs. $\%HbO_2$ for the resting and active blood volumes, and spans a $\%HbO_2$ range from 0.6 (resting) to 0.75 (active). For the resting state blood volume, ΔR_2^* (difference between 60% blood oxygen saturation and 100% blood oxygen saturation) was about $1.32\,s^{-1}$. During activation, considering changes in blood oxygen saturation only, the value of ΔR_2^* decreased along the same curve, to $0.5\,s^{-1}$, a difference of $-0.82\,s^{-1}$ (activation-induced signal change of 3.3% at a TE of 40 ms). If changes in blood volume are considered, the ΔR_2^* value is measured at the same blood oxygenation, but on the curve representing the higher blood volume. Here, the ΔR_2^* value was about $0.62\,s^{-1}$, a difference of $-0.70\,s^{-1}$ (an activation-induced signal change of 2.8% at a TE of 40 ms). In general, the small increase in blood volume caused a small reduction in the activation-induced signal increase, but the increase in blood oxygenation dominated.

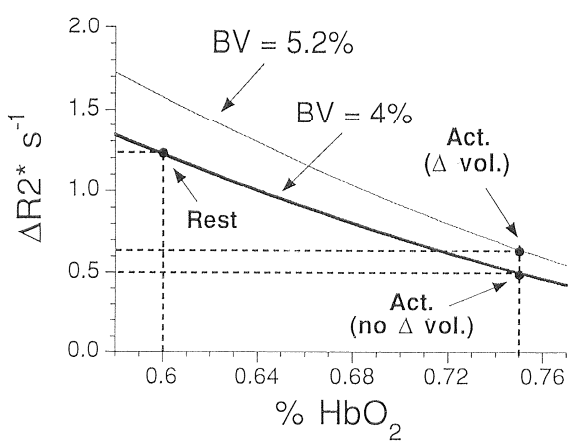

Figure 27. Hypothesized activation-induced changes in blood volume and oxygenation. The effect of an increase in oxygenation and blood volume is opposite in sign, but the oxygenation effect dominates.

V. DISCUSSION AND CONCLUSIONS

These simulations serve to clarify the mechanisms underlying activation-induced MR signal changes. The simulation methodology presented here provides a flexible and computationally efficient alternative to Monte Carlo techniques. In these simulations, we assessed the significance of physiologic and biophysical parameters on activation-induced changes in R_2^* and R_2.

The simulation method was first compared with a Monte Carlo modeling method [1] and gave strongly matching results. Second, when using approximate estimates of physiologic and biophysical phenomena during resting and activated states, we obtained general agreement between simulated and measured ΔR_2 and ΔR_2^* values [16, 17, 19–22, 58, 65]. These results support the hypothesis that activation-induced signal changes can be explained primarily by a bulk susceptibility contrast mechanism.

More specific conclusions can also be made. The first is that modulation of resting state blood volume and of field strength had the strongest effects on the ΔR_2^* and ΔR_2 values. This conclusion has important implications for FMRI. Blood volume varies considerably from voxel to voxel. These variations across voxels likely modulate FMRI signal change magnitude more strongly than spatial differences in activation-induced oxygenation changes. For example, a large vessel "downstream" from an activated region, filling a voxel, may experience a much smaller oxygenation change than the capillaries and venuoles in the immediate vicinity of the activated region but, because of the large blood volume in that particular voxel, may still show the largest activation-induced signal change for both spin-echo and gradient-echo sequences. These "large vessel effects" have been alluded to by several investigators [60, 69–72]. Methods for removing

these effects have ranged from vein identification methods [58, 60, 69–71, 73, 74] to normalization of activation-induced signal change maps to a blood volume map created by global vasodilatation accompanying hypercapnia [75].

The strong simulated field strength dependence indicates that a gain in functional contrast can be obtained by performing functional imaging at high fields. Experimental evidence is conflicting; both $B_o^{0.8}$ [20] and $B_o^{1.6}$ dependencies [76] of activation-induced ΔR_2^* have been reported. The stronger B_o dependence of the smaller radii vessels may indicate that at higher field strengths, smaller compartments (capillaries and red blood cells) may contribute more predominantly.

The second specific conclusion that can be made is that the modulation of the diffusion coefficient and compartment size radius had the greatest effect on the $\Delta R_2^*/\Delta R_2$ ratio. Experimental studies have observed large spatial heterogeneity in $\Delta R_2^*/\Delta R_2$ [17, 58, 77], suggesting a large heterogeneity in predominant compartment size or diffusion coefficient. The average ratio measured in vivo is in the range of 3/1 to 4/1 [16, 18–20, 58, 65], suggesting with the assumed proton dynamics and susceptibilities that the "average" compartment size is about 8–10 μm.

Modulation of field strength did not strongly affect the simulated $\Delta R_2^*/\Delta R_2$ values. These results are also in approximate agreement with preliminary experimental studies [18, 20].

Finally, this model demonstrates that even though blood oxygenation and blood volume increases during activation cause opposite sign effects, blood oxygenation changes dominate the signal change. This effect should not be confused with the strong effect that resting state blood volume has on ΔR_2^* and ΔR_2, given an oxygenation change and fixed volume.

Currently, four classes of BOLD models have been published. The first class is that which only takes into consideration the dephasing effects on extravascular spins by gradients outside the simulated vessels [1–3, 8, 63]. The second class is that which takes into consideration the intravascular phase shift effect, neglecting the effects of external gradients on dephasing [78]. In this second class, the cause for intravoxel dephasing is the phase difference that accrues between the intravascular spins and extravascular spins. The third class is a combination of the first two classes, taking into consideration both the external gradient dephasing effects and the internal phase shift effects. The deterministic diffusion model presented in this report falls into this third class. The fourth class is identical to the third class; in addition, however, intravascular dephasing due to red blood cell effects on blood plasma spins is also considered [5–7, 9]. It appears that this fourth class is the most realistic class of models so far. Currently, work is being performed to incorporate intravascular dephasing effects into the deterministic diffusion model presented.

The ultimate goal of all FMRI contrast models is a complete understanding of the variables that contribute to the signal changes such that accurate localization of brain activation can be made; quantification of flow, volume, and oxygenation changes can be made, and other useful neuronal, hemodynamic, or biophysical information can be obtained. Both careful experimentation and modelling are essential to achieve this goal. The science and art of FMRI interpretation is advanced at each iterative step of this experimentation and modeling process.

ACKNOWLEDGMENTS

The authors extend thanks to Jerry Boxerman, Timothy Davis, Kathleen Donahue, Andrew Greene, Scott Hinks, James Hyde, Andrej Jesmanowicz, Ken Kwong, Bruce Rosen, Elliot Stein, and Robert Weisskoff for enlightening discussions regarding this work.

REFERENCES

1. S. Ogawa, R. S. Menon, D. W. Tank, S.-G. Kim, H. Merkle, J. M. Ellerman, and K. Ugurbil, "Functional brain mapping by blood oxygenation level-dependent contrast magnetic resonance imaging: A comparison of signal characteristics with biophysical model," *Biophys. J.* **64**, 803–812 (1993).
2. R. M. Weisskoff, C. S. Zuo, J. L. Boxerman, and B. R. Rosen, "Microscopic susceptibility variation and transverse relaxation: Theory and experiment," *Magn. Res. Med.* **31**, 601–610 (1994).
3. R. M. Weisskoff, J. L. Boxerman, C. S. Zuo, and B. R. Rosen, "Endogenous susceptibility contrast: principles of relationship between blood oxygenation and MR signal charge," in *Functional MRI of the Brain*. Society of Magnetic Resonance in Medicine, Berkeley, 1993, p. 103.
4. R. P. Kennan, J. Zhong, and J. C. Gore, "Intravascular susceptibility contrast mechanisms in tissues," *Magn. Res. Med.* **31**, 9–21 (1994).
5. D. A. Yablonsky and E. M. Haacke, "Theory of NMR signal behavior in magnetically inhomogeneous tissues: the static dephasing regime," *Magn. Res. Med.* **32**, 749–763 (1994).
6. J. L. Boxerman, P. A. Bandettini, K. K. Kwong, J. R. Baker, T. L. Davis, B. R. Rosen, and R. M. Weisskoff, "The intravascular contribution to FMRI signal change: Monte Carlo modeling and diffusion-weighted studies in vivo," *Magn. Res. Med.* **34**, 4–10 (1995).
7. J. L. Boxerman, R. M. Weisskoff, K. K. Kwong, T. L. Davis, and B. R. Rosen, "The intravascular contribution to FMRI signal change. Modeling and diffusion-weighted in vivo studies," in *Proc., Society of Magnetic Resonance, 2nd Annual Meeting, San Francisco, 1994,*" p. 619.
8. J. L. Boxerman, R. M. Weisskoff, B. E. Hoppel, and B. R. Rosen, "MR contrast due to microscopically heterogeneous magnetic susceptibility: cylindrical geometry," in *Proc., Society of Magnetic Resonance in Medicine, 12th Annual Meeting, New York, 1993*, p. 389.
9. J. L. Boxerman, L. M. Hamberg, B. R. Rosen, and R. M. Weisskoff, "MR contrast due to intravascular magnetic susceptibility perturbations," *Magn. Res. Med.* (in press).
10. E. C. Wong and P. A. Bandettini, "A deterministic method for computer modelling of diffusion effects in MRI with application to BOLD contrast imaging," in *Proc., Society of Magnetic Resonance in Medicine, 12th Annual Meeting, New York, 1993*, p. 10.
11. R. M. Weisskoff and S. Kiihne, "MRI susceptometry: Image-based measurement of absolute susceptibility of MR contrast agents and human blood," *Magn. Res. Med.* **24**, 375–383 (1992).
12. H. Forster, personal communication.
13. L. Stryer, *Biochemistry*, W. H. Freeman and Company, New York, 1981.
14. J. R. Pappenheimer, "Passage of molecules through capillary walls," *Physiol. Rev.* **33**, 387 (1953).
15. H. M. Duvernoy, S. Delon, and J L. Vannson, "Cortical blood vessels of the human brain," *Brain Res. Bull.* **7**, 519–579 (1981).
16. P. A. Bandettini, E. C. Wong, R. S. Hinks, L. Estkowski, and J. S. Hyde, "Quantification of changes in relaxation rates R_2^* and R_2 in activated brain tissue," in *Proc., Society of Magnetic Resonance in Medicine, 11th Annual Meeting, Berlin, 1992*, p. 719.

17. P. A. Bandettini, E. C. Wong, A. Jesmanowicz, R. S. Hinks, and J. S. Hyde, "Simultaneous mapping of activation-induced ΔR_2^* and ΔR_2 in the human brain using a combined gradient-echo and spin-echo EPI pulse sequence," in *Proc., Society of Magnetic Resonance in Medicine, 12th Annual Meeting, New York, 1993*, p. 169.
18. A. Jesmanowicz, P. A. Bandettini, E. C. Wong, G. Tan, and J. S. Hyde, "Spin-echo and gradient-echo EPI of human brain function at 3 Tesla," in *Proc., Society of Magnetic Resonance in Medicine, 12th Annual Meeting, New York, 1993*, p. 1390.
19. P. A. Bandettini, E. C. Wong, A. Jesmanowicz, R. S. Hinks, and J. S. Hyde, "Spin-echo and gradient-echo EPI of human brain activation using BOLD contrast: A comparative study at 1.5 Tesla," *NMR Biomed.* **7**, 12–19 (1994).
20. P. A. Bandettini, E. C. Wong, A. Jesmanowicz, R. Prost, R. W. Cox, R. S. Hinks, and J. S. Hyde, "MRI of human brain activation at 0.5 T, 1.5 T, and 3 T: Comparisons of ΔR_2^* and functional contrast to noise ratio," in *Proc., Society of Magnetic Resonance, 2nd Annual Meeting, San Francisco, 1994*, p. 434.
21. B. E. Hoppel, J. R. Baker, R. M. Weisskoff, and B. R. Rose, "The dynamic response of ΔR_2 and $\Delta R_2'$ during photic activation," in *Proc., Society of Magnetic Resonance in Medicine, 12th Annual Meeting, New York, 1993*, p. 1384.
22. B. E. Hoppel, R. M. Weisskoff, K. R. Thulborn, J. B. Moore, K. K. Kwong, and B. R. Rosen, "Measurement of regional blood oxygenation and cerebral hemodynamics," *Magn. Res. Med.* **30**, 715–723 (1993).
23. G. Mchedlishvili, *Arterial Behavior and Blood Circulation in the Brain*, Plenum Press, New York, 1986.
24. D. Le Bihan, R. Turner, C. T. Moonen, and J. Pekar, "Imaging of diffusion and microcirculation with gradient sensitization: Design, strategy, and significance," *Journal of Magnetic Resonance Imaging* **1**, 7–28 (1991).
25. R. Mills, "Self-diffusion in normal and heavy water in the range 1–45°," *J. Phys. Chem.* **77**, 685–688 (1975).
26. D. Le Bihan and R. Turner, "Intravoxel incoherent motion imaging using spin-echoes," *Magn. Res. Med.* **19**, 221–227 (1991).
27. P. E. Roland, *Brain Activation*, Wiley-Liss, New York, 1993.
28. C. S. Roy and C. S. Sherrington, "On the regulation of the blood-supply of the brain," *J. Physiol* **11**, 85–108 (1890).
29. F. Gotoh and K. Tanaka, in *Handbook of Clinical Neurology*. P. J. Vinkin, G. W. Bruyn, and H. L. Klawans, Eds., Elsevier Science Publishing, New York, 1987, p. 47.
30. W. Kushinsky, "Coupling between functional activity, metabolism, and blood flow in the brain: State of the art," *Microcirculation* **2**, 357–378 (1982–1983).
31. D. W. Busija and D. D. Heistad, *Factors Involved in the Physiological Regulation of the Cerebral Circulation*, Springer-Verlag, Berlin, 1984.
32. M. Ursino, "Mechanisms of cerebral blood flow regulation," *Crit. Rev. Biomed. Eng.* **18**, 255–288 (1991).
33. H. C. Lou, L. Edvinsson, and E. T. MacKenzie, "The concept of coupling blood flow to brain function: Revision required?" *Ann. Neurol.* **22**, 289–297 (1987).
34. W. Kuschinsky, "Physiology of cerebral blood flow and metabolism," *Arzneimittelforschung* **41**, 284–288 (1991).
35. Y. E. Moskalenko, G. B. Weinstein, I. T. Demchenko, Y. Y. Kislyakov, and A. I. Krivchenko, *Biophysical Aspects of Cerebral Circulation*, Pergamon Press, Oxford, 1980.
36. C. Estrada, E. Mengual, and C. Gonzalez, "Local NADPH-diaphorase neurons innervate pial arteries and lie close or project to intracerebral blood vessels: A possible role for nitric oxide in the regulation of cerebral blood flow," *J. Cereb. Blood Flow Metab.* **13**, 978–984 (1993).
37. U. Dirnagl, U. Lindauer, and A. Villringer, "Role of nitric oxide in the coupling of cerebral blood flow to neuronal activation in rats," *Neurosci. Lett.* **149**, 43–46 (1993).
38. C. Iadecola, Regulation of cerebral microcirculation during neural activity: Is nitric oxide the missing link? *Trends Neurosci.* **16**, 206–214 (1993).
39. D. H. Ingvar, "Patterns of brain activity revealed by measurements of regional cerebral blood flow," in *Brain Work*. D. H. Ingvar and N. A. Lassen, Eds., Munksgaard, Copenhagen, 1975, p. 397.
40. S. T. Grafton, R. P. Woods, J. C. Mazziotta, and M. E. Phelps, "Somatotopic mapping of the primary motor cortex in humans: Activation studies with cerebral blood flow and positron emission tomography," *J. Neurophysiol.* **66**, 735–743 (1991).
41. J. G. Colebatch, M.-P. Deiber, R. E. Passingham, K. J. Friston, and R. S. J. Frackowiack, "Regional cerebral blood flow during voluntary arm and hand movements in human subjects," *J. Neurophysiol.* **65**, 1392–1401 (1991).
42. P. T. Fox and M. E. Raichle, "Stimulus rate determines regional brain blood flow in striate cortex," *Ann. Neurol.* **17**, 303–305 (1985).
43. O. G. Cameron, J. G. Modell, R. D. Hichwa, B. W. Agranoff, and R. A. Koeppe, "Changes in sensory-cognitive input: Effects on cerebral blood flow," *J. Cereb. Blood Flow Metab.* **10**, 38–42 (1990).
44. P. T. Fox and M E. Raichle, "Stimulus rate dependence of regional cerebral blood flow in human striate cortex, demonstrated by positron emission tomography," *J. Neurophysiol.* **51**, 1109–1120 (1991).
45. C. A. Sandman, J. P. O'Halloran, and R. Isenhart, "Is there an evoked vascular response?" *Science* **224**, 1355–1356 (1984).
46. J. W. Belliveau, D. N. Kennedy, R. C. McKinstry, B. R. Buchbinder, R. M. Weisskoff, M. S. Cohen, J. M. Vevea, T. J. Brady, and B. R. Rosen, "Functional mapping of the human visual cortex by magnetic resonance imaging," *Science* **254**, 716–719 (1991).
47. A. Villringer, J. Planck, C. Hock, L. Scheinkofer, and U. Dirnagl, "Near infrared spectroscopy (NIRS): A new tool to study hemodynamic changes during activation of brain function in human adults," *Neurosci. Lett.* **154**, 101–104 (1993).
48. P. T. Fox and M. E. Raichle, Focal physiological uncoupling of cerebral blood flow and oxidative metabolism during somatosensory stimulation in human subjects," *Proc. Natl. Acad. Sci. USA* **83**, 1140–1144 (1986).
49. R. D. Frostig, "!E. E. Lieke, D. Y. Ts'o, and A. Grinvald, "Cortical functional architecture and local coupling between neuronal activity and the microcirculation revealed by in vivo high-resolution optical imaging of intrinsic signals," *Proc. Natl. Acad. Sci. USA* **87**, 6082–6086 (1990).
50. A. Grinvald, R. D. Frostig, R. M. Siegel, and E. Bratfeld, "High-resolution optical imaging of functional brain architecture in the awake monkey," *Proc. Natl. Acad. Sci. USA* **88**, 11559–11563 (1991).
51. R. D. Frostig, "What does in vivo optical imaging tell us about the primary visual cortex in primates?" in *Cerebral Cortex*, Vol. 10. A. Peters and K. S. Rockland, Eds., Plenum Press, New York, 1994, p. 331.
52. R. L. Grubb, M. E. Raichle, J. O. Eichling, and M. M. Ter-Pogossian, "The effects of changes in $PaCO_2$ in cerebral blood volume, blood flow, and vascular mean transit time," *Stroke* **5**, 630–639 (1974).
53. J. A. Detre, J. S. Leigh, D. S. Williams, and A. P. Koretsky, "Perfusion imaging," *Magn. Res. Med.* **23**, 37–45 (1992).
54. D. S. Williams, J. A. Detre, J. S. Leigh, and A. S. Koretsky, "Magnetic resonance imaging of perfusion using spin-inversion of arterial water," *Proc. Natl. Acad. Sci. USA* **89**, 212–216 (1992).
55. J. A. Detre, W. Zhang, D. A. Roberts, A. C. Silva, D. S. Williams, D. J. Grandis, A. P. Koretsky, and J S. Leigh, "Tissue-

specific perfusion imaging using arterial spin labeling," *NMR Biomed.* **7**, 75–82 (1994).
56. K. K. Kwong, J. W. Belliveau, D. A. Chesler, I. E. Goldberg, R. M. Weisskoff, B. P. Poncelet, D. N. Knnedy, B. E. Hoppel, M. S. Cohen, R. Turner, H. M. Cheng, T. J. Brady, and B. R. Rosen, "Dynamic magnetic resonance imaging of human brain activity during primary sensory stimulation," *Proc. Natl. Acad. Sci. USA* **89**, 5675–5679 (1992).
57. R. R. Edelman, B. Sievert, P. Wielopolski, J. Pearlman, and S. Warach, "Noninvasive mapping of cerebral perfusion by using EPISTAR MR angiography," *Journal of Magnetic Resonance Imaging* **4**, 68 (1994) [abstr.].
58. P. A. Bandettini, E. C. Wong, R. W. Cox, A. Jesmanowicz, R. S. Hinks, and J. S. Hyde, "Simultaneous assessment of blood oxygenation and flow contributions to activation induced signal changes in the human brain," in *Proc., Society of Magnetic Resonance, 2nd Annual Meeting, San Francisco, 1994*, p. 621.
59. J. H. Duyn, C. T. W. Moonen, G. H. van Yperen, R. W. d. Boer, and P. R. Luyten, "Inflow versus deoxyhemoglobin effects in BOLD functional MRI using gradient-echoes at 1.5 T," *NMR Biomed.* **7**, 83–88 (1994).
60. J. Frahm, K.-D. Merboldt, W. Hanicke, A. Kleinschmidt, and H. Boecker, "Brain or vein-oxygenation or flow? On signal physiology in functional MRI of human brain activation," *NMR Biomed.* **7**, 45–53 (1994).
61. S. C.-K. Chu, Y. Xu, J. A. Balschi, C. S. Springer Jr., "Bulk magnetic susceptibility shifts in NMR studies of compartmentalized samples: use of paramagnetic reagents," *Magn. Res. Med.* **13**, 239–262 (1990).
62. C. R. Fisel, J. L. Ackerman, R. B. Buxton, L. Garrido, J. W. Belliveau, B. R. Rosen, and T. J. Brady, "MR contrast due to microscopically heterogeneous magnetic susceptibility: Numerical simulations and appliations to cerebral physiology," *Magn. Res. Med.* **17**, 336–347 (1991).
63. R. M. Weisskoff, B. J. Hoppel, and B. R. Rosen, "Signal changes in dynamic contrast studies: Theory and experiment in vivo. *Journal of Magnetic Resonance Imaging* **2**, 77 (1992) [abstr.].
64. L. Ott, *An Introduction to Statistical Methods and Data Analysis*, Duxbury Press, Boston, 1984.
65. P. A. Bandettini, E. C. Wong, L. Estkowski, R. S. Hinks, and J. S. Hyde, "Spin-echo echo-planar imaging of localized signal enhancement in the human brain during task activation," *Journal of Magnetic Resonance Imaging* **3**, 63 (1993) [abstr.].
66. P. Gilles, S. Peto, F. Moiny, J. Mispelter, and C.-A. Cuenod, "Proton transverse nuclear magnetic relation in oxidized blood: A numerical approach," *Magn. Res. Med.* **33**, 93–100 (1995).
67. K. R. Thulborn, J. C. Waterton, P. M. Matthews, and G. K. Radda, "Oxygenation dependence of the transverse relaxation time of water protons in whole blood at high field," *Biochim. Biophys. Acta* **714**, 265–270 (1982).
68. G. A. Wright, B. S. Hu, and A. Macovski, "Estimating oxygen saturation of blood in vivo with MR imaging at 1.5 T," *Journal of Magnetic Resonance Imaging* **1**, 275–283 (1991).
69. A. T. Lee, C. H. Meyer, and G. H. Glover, "Discrimination of large veins in time-course functional neuroimaging with spiral k-space tarjectories," *Journal of Magnetic Resonance Imaging* **3**, 59–60 (1993) [abstr.].
70. R. S. Monon, S. Ogawa, D. W. Tank, and K. Ugurbil, "4 Tesla gradient recalled echo characteristics of photic stimulation-induced signal changes in the human primary visual cortex," *Magn. Res. Med.* **30**, 380–386 (1993).
71. S.-G. Kim, K. Hendrich, X. Hu, H. Merkle, and K. Ugurbil, "Potential pitfalls of functional MRI using conventional gradient-recalled echo techniques," *NMR Biomed.* **7**, 69–74 (1994).
72. R. Turner, P. Jezzard, D. L. Bihan, and A. Prinster, "Contrast mechanisms and vessel size effects in BOLD contrast functional neuroimaging," in *Proc., Society of Magnetic Resonance in Medicine, 12th Annual Meeting, New York, 1993*, p. 173.
73. A. T. Lee, G. H. Glover, and C. H. Meyer, "Discrimination of large venous vessels in time-course spiral blood-oxygen-level-dependent magnetic-resonance functional neuroimaging," *Magn. Res. Med.* **33**, 745–754 (1995).
74. S. Lai, A. L. Hopkins, E. M. Haacke, D. Li, B. A. Wasserman, P. Buckley, L. Friedman, H. Meltzer, P. Hedera, and R. Friedland, "Identification of vascular structures as a major source of signal contrast in high resolution 2D and 3D functional activation imaging of the motor cortex at 1.5 T: Preliminary results," *Magn. Res. Med.* **30**, 387–392 (1993).
75. P. A. Bandettini, A. E. Aaron, E. C. Wong, T. F. Lowry, R. S. Hinks, J. S. Hyde, and H. V. Forster, "Hypercapnia and hypoxia in the human brain: Effects on resting and activation-induced MRI signal," in *Proc., Society of Magnetic Resonance, 2nd Annual Meeting, San Francisco, 1994*, p. 700.
76. R. Turner, P. Jezzard, H. Wen, K. K. Kwong, D. L. Bihan, T. Zeffiro, and R. S. Balaban, "Functional mapping of the human visual cortex at 4 and 1.5 Tesla using deoxygenation contrast EPI," *Magn. Res. Med.* **29**, 277–279 (1993).
77. A. Prinster, C. Pierpaoli, P. Jezzard, and R. Turner, "Simultaneous measurement of ΔR_2 and ΔR_2^* in cat brain during hypoxia and hypercapnia," in *Proc., Society of Magnetic Resonance, 2nd Annual Meeting, San Francisco, 1994*, p. 439.
78. E. M. Haacke, A. Hopkins, S. Lai, P. Buckley, L. Friedman, H. Meltzer, P. Hedera, R. Friedland, L. Thompson, D. Detterman, J. Tkach, and J. S. Lewin, "2D and 3D high resolution gradient-echo functional imaging of the brain: Venous contributions to signal in motor cortex studies," *NMR Biomed.* **7**, 54–62 (1994).